Chemical Geology 688 (2025) 122810

Contents lists available at ScienceDirect

Chemical Geology

journal homepage: www.elsevier.com/locate/chemgeo

Research Paper

Tracking the transition from magmatic to post-crystallization environment in the Sesia Magmatic System (Italy) by coupling quartz OH-defects and trace element analyses

G. Tumaini [a,1], L. Tavazzani [b,*,1], H. Skogby [c], F. Bernardi [a], S. Sinigoi [a], D. Lenaz [a]

[a] Department of Mathematics, Informatics and Geosciences, University of Trieste, 34128 Trieste, Italy
[b] Institute of Geochemistry and Petrology, ETH Zürich, CH-8092 Zürich, Switzerland
[c] Department of Geosciences, Swedish Museum of Natural History, Box 50007, SE-10405 Stockholm, Sweden

ARTICLE INFO

Editor: Marco Fiorentini

Keywords:
FTIR
LA-ICP-MS
Lithium
Diffusion
Granite
Ivrea-Verbano Zone
Volcanic-plutonic connection

ABSTRACT

The production of a significant thermal and fluid anomaly during the assembly of large magmatic bodies inevitably leads to a prolonged, post-magmatic evolution of the system. To shed light on the transition between magmatic and post-crystallization environment, we investigated the variation of OH-defects and trace elements content in quartz from intrusive and eruptive products of the Sesia Magmatic System (SW Alps, Italy). Specifically, quartz crystals were sampled from a floor-to-roof section of the Valle Mosso Pluton and two rhyolitic units of the Sesia Caldera, which represents the crystallized remnants of a magmatic plumbing system beneath a large Permian caldera. A total of 120 quartz crystals were analysed using Fourier Transform InfraRed (FTIR) spectroscopy to investigate OH-defects both quantitatively and qualitatively and Laser Ablation-Inductively Coupled Plasma-Mass Spectrometry (LA-ICP-MS) to assess trace element abundances. Results indicate systematic variations: (1) intrusive quartz shows gradual decrease in Ti and increase in total defect water content (1–25 ppm), following the differentiation degree; (2) volcanic quartz displays variable Ti and water contents (2–14 ppm) comparable to those of the intrusive lithologies; (3) in both intrusive and eruptive units, lattice-bound Al-specific defects dominate over non-lattice bound Li-specific defects, except in a porphyritic dike showing evidence of fast cooling. Our findings suggest that, in absence of fast cooling, slow-diffusing elements and lattice-bound OH-defects (e.g. Al, Ti, AlOH) preserve primary magmatic signals, while fast-diffusing elements (e.g. Li) and interstitial defects (e.g. LiOH) provide insights into post-crystallization histories. The combined analysis of these features offers a powerful tool for reconstructing the thermal and chemical evolution of magmatic systems, from magma chamber processes to post-eruptive alteration. Moreover, it provides insights on the robustness of quartz OH-defects and trace element inventory as a tool for provenance indicator.

1. Introduction

Quartz is a Nominally Anhydrous Mineral (NAM) and a major constituent of upper crustal felsic igneous rocks (e.g. granites, rhyolites). Although typically regarded as a pure mineral, quartz can incorporate trace amounts of chemical impurities into its crystal lattice, such as P^{5+}, Ti^{4+}, Ge^{4+}, Al^{3+}, Fe^{3+}, B^{3+}, Li^{+}, Na^{+}, K^{+} and H^{+} (Bambauer, 1961; Kats, 1962; Bambauer et al., 1963; Aines and Rossman, 1984; Müller and Koch-Müller, 2009; Götze et al., 2021). These cations may be incorporated through either the exchange of cations isovalent to Si^{4+} (e.g. Ti^{4+}, Ge^{4+}) or through coupled substitutions, most often as a combination of mono- and tri-valent cations (e.g. $Si^{4+} \leftrightarrow Al^{3+} + H^{+}$ or $Si^{4+} \leftrightarrow B^{3+} + H^{+}$; Botis and Pan, 2009). The involvement of hydrogen in the substitution process can result in the formation of hydroxyl dipoles (OH^{-}) with the oxygen anions of the quartz lattice, giving rise to OH-defects. Other H^{+} assimilation mechanisms include the incorporation of interstitial molecules, such as the neutral species LiOH (Kats, 1962; Bambauer et al., 1963), which has been experimentally shown to be negatively correlated to pressure and to be favourable at high Li contents (Frigo et al., 2016).

The OH dipoles can be detected and distinguished depending on the charge compensation by their absorption frequency in the IR range of electromagnetic radiation. Fourier Transform Infrared (FTIR)

* Corresponding author.
E-mail address: lorenzo.tavazzani@eaps.ethz.ch (L. Tavazzani).
[1] These authors contributed equally to this work.

https://doi.org/10.1016/j.chemgeo.2025.122810
Received 21 February 2025; Received in revised form 19 April 2025; Accepted 23 April 2025
Available online 8 May 2025

spectroscopy is a widely applied method for qualitatively and quantitatively investigating hydrous defects in NAMs (Stalder and Neuser, 2013). In parallel, Laser Ablation-Inductively Coupled Plasma-Mass Spectrometry (LA-ICP-MS) is routinely employed for investigating trace element contents in quartz due to its high sensitivity and low detection limits (Ackerson et al., 2015).

The development of a method to identify and quantify OH-defects (Stalder and Konzett, 2012) has opened the way to a deeper understating of the relationship between OH-defects and petrological conditions. Notably, the physical and chemical parameters at play during magma crystallization (e.g. pressure, temperature, chemical composition, trace element availability, and water fugacity) exhort a crucial role in both OH-defect formation in quartz and trace element incorporation (e.g. Suzuki and Nakashima, 1999; Frigo et al., 2016; Potrafke et al., 2020). Given OH-defects sensitivity to physico-chemical parameters, FTIR studies of OH-defects have been employed as a tool for detrital quartz in provenance studies, enabling an approximate distinction between sedimentary, igneous, and metamorphic sources (Stalder and Neuser, 2013; Stalder, 2014; Stalder et al., 2017, 2019; Jaeger et al., 2019; Bernardi et al., 2022; Bernardi, 2024). In the last decade, a series of systematic studies have been conducted on quartz grains from metamorphic (Müller and Koch-Müller, 2009), volcanic (Biró et al., 2016, 2017; Tollan et al., 2019; Jollands et al., 2020a), and plutonic (Müller et al., 2009; Stalder et al., 2017; Potrafke et al., 2020) rocks. Recent studies have also included study of OH-defects in experimentally grown quartz from haplogranitic systems (Baron et al., 2015; Frigo et al., 2016; Potrafke et al., 2019). In parallel, the versatility and relative ease of use of LA-ICP-MS techniques have led to numerous comprehensive studies on quartz trace-elements composition from various geological settings including granites (Jacamon and Larsen, 2009; Larsen et al., 2009; Breiter et al., 2013; Ackerson et al., 2015; Drivenes et al., 2016; Breiter et al., 2020; Zhang et al., 2022; Ji et al., 2024), pegmatites (Götze et al., 2004; Larsen et al., 2004; Müller et al., 2008; Beurlen et al., 2011; Breiter et al., 2014; Müller et al., 2015; Garate-Olave et al., 2017; Müller et al., 2021; Keyser et al., 2023; Zhou et al., 2023; Sittner et al., 2024), volcanic rocks (Breiter et al., 2012; Audétat, 2013), hydrothermal deposits (Takahashi et al., 2007; Rusk et al., 2008; Götte et al., 2011; Müller et al., 2018; Pacák et al., 2019; Peterková and Dolejš, 2019; Fu et al., 2020; Lan et al., 2021; Rottier and Casanova, 2021; Rottier et al., 2021; Zhang et al., 2022; Hong et al., 2024), and metamorphic lithologies (Monecke et al., 2002; Müller and Koch-Müller, 2009).

Nonetheless, with the notable exception of the study from Potrafke et al. (2020) on tin-bearing granitic bodies of Zinnwald and Podlesí, detailed investigations on the paired evolution of hydrous defect and trace elements of quartz from individual igneous bodies are lacking. Moreover, there are to date no studies on OH-defects budget in geologic settings that include coeval and cogenetic plutonic-volcanic pairs. To bridge this gap, we present the findings of a systematic investigation into the paired variation of OH-defects and trace element contents in magmatic quartz from the intrusive and volcanic silicic products of a well-known Permian transcrustal plumbing (i.e. Sesia Magmatic System; Quick et al., 2009; Sinigoi et al., 2010, Tavazzani et al., 2020). The objective of this research is to characterise the magmatic system using the combination of two analytical techniques, FTIR and LA-ICP-MS. This will validate potential relationships between trace element contents and OH-defects formation in both the magmatic and post-crystallization environment. In addition, this work provides a more comprehensive calibration and evaluation of the possible limitations of the OH tool in provenance studies of sedimentary quartz.

2. Geological setting

2.1. Sesia Magmatic System

The Permian Sesia Magmatic System (SMS; Sinigoi et al., 2010) is located in a virtually complete section of pre-Mesozoic continental crust exposed in the South-Western Alps (Italy) and represents the crystallized remnants of a magmatic plumbing system beneath a Permian caldera (Quick et al., 2009; Karakas et al., 2019). This crustal section encompasses the deep crustal Ivrea-Verbano Zone (IVZ) and the upper crustal Serie dei Laghi (SdL) domains (Fountain, 1976; Handy and Zingg, 1991; Henk et al., 1997; Rutter et al., 1999; Connop et al., 2024). The SMS is comprised of three main coeval igneous units: the Mafic Complex, which intruded the deep crustal Ivrea-Verbano Zone (8 to 5 kbar; Demarchi et al., 1998), the Valle Mosso-Roccapietra granitic pluton, which intruded the upper crust (4 to 2 kbar; Tavazzani et al., 2020, 2023) and the Sesia Caldera (SC), characterised by a volcanic field primarily featuring caldera-fill rhyolitic deposits (Quick et al., 2009).

2.2. Valle Mosso Pluton

The pre-Permian Serie dei Laghi formation hosts numerous granitic plutons, collectively known as Graniti dei Laghi, among which is the Valle Mosso-Roccapietra Pluton (Boriani et al., 1988). This intrusion is subdivided into two discrete granitic bodies by an alpine shear-zone, the Cremosina Line. Among these two bodies, the Valle Mosso Pluton (VMP) is located south of the Cremosina Line and consists of a suite of cogenetic intrusive rocks, varying from quartz-monzonite to high-silica leucogranite (65–77 wt% SiO_2; Zezza, 1977; Tavazzani et al., 2017, 2020). Further classification of the VMP entails the subdivision into five north-south elongated intrusive units based on a combination of lithological, textural, and compositional characteristics (Tavazzani et al., 2017, 2020) (Fig. 1a-b).

The westernmost sector (quartz-monzonite unit; Gd; unit labels are summarized in Fig. 1a and Table 1) is in primary contact with the polymetamorphic Kinzigite Formation (Zezza, 1977) and has been interpreted as the floor of the intrusion (Tavazzani et al., 2017). This unit is characterised by coarse-grained quartz-monzonite, grading eastward into a monzogranite, occasionally displaying macroscopic foliation resulting from the alignment of biotite and amphibole (Tavazzani et al., 2020). This unit represents the least evolved unit, with a silica content of 67–72 wt% SiO_2 (Tavazzani et al., 2020). Directly to the east of the quartz-monzonite unit lies a more markedly porphyritic monzogranite unit (Pg), characterised by the presence of K-feldspar (grain size 1–4 cm) and quartz (grain size 0.5–1 cm) phenocrysts embedded within a medium- to fine-grained matrix (Tavazzani et al., 2017, 2020). Within this unit resides a microgranitic porphyry (Gp) unit, which forms an isolated NNW-elongated intrusive body (0.5 km^2) consisting of a fine-grained to aphanitic matrix, and a variable phenocrysts content (5–45 vol%; namely K-feldspar, plagioclase, biotite, and quartz). This unit is rich in microgranular mafic enclaves (up to 10 vol%) of variable composition and shows widespread petrographic evidence of mixing between silicic and mafic melts and rapid cooling (Tavazzani et al., 2020). Moving eastward, the porphyritic monzogranite gradually transitions into a homogeneous coarse-grained monzogranite unit (Hwg). This unit exhibits a more evolved composition, with up to 74 wt% SiO_2 (Tavazzani et al., 2020). Finally, at the easternmost edge of the intrusion, the homogeneous monzogranite unit grades into a coarse-grained homogeneous pink leucogranite (Hpg), marked by the vibrant pink colouring of K-feldspars due to extensive kaolinization and precipitation of cryptocrystalline hematite (Zezza, 1977; Tavazzani et al., 2020). The leucogranite body represents the most evolved unit of the VMP with silica content reaching up to 76.5 wt% SiO_2 (Tavazzani et al., 2020). This unit intrudes the volcanic pile of the Sesia Caldera, which locally experienced contact metamorphism (Sbisà, 2009). As the boundary with the volcanic rocks is approached, evidence of widespread fluid activity (i.e. pegmatitic veins and pockets, quartz dikes, and miarolitic cavities) becomes increasingly abundant (Tavazzani et al., 2020).

The overall features, textures, and bulk-rock composition of the VMP indicate the evolution of a silicic magma chamber experiencing prolonged differentiation, primarily influenced by crystal-melt segregation and occasionally replenished by granitic and/or mafic magma injections

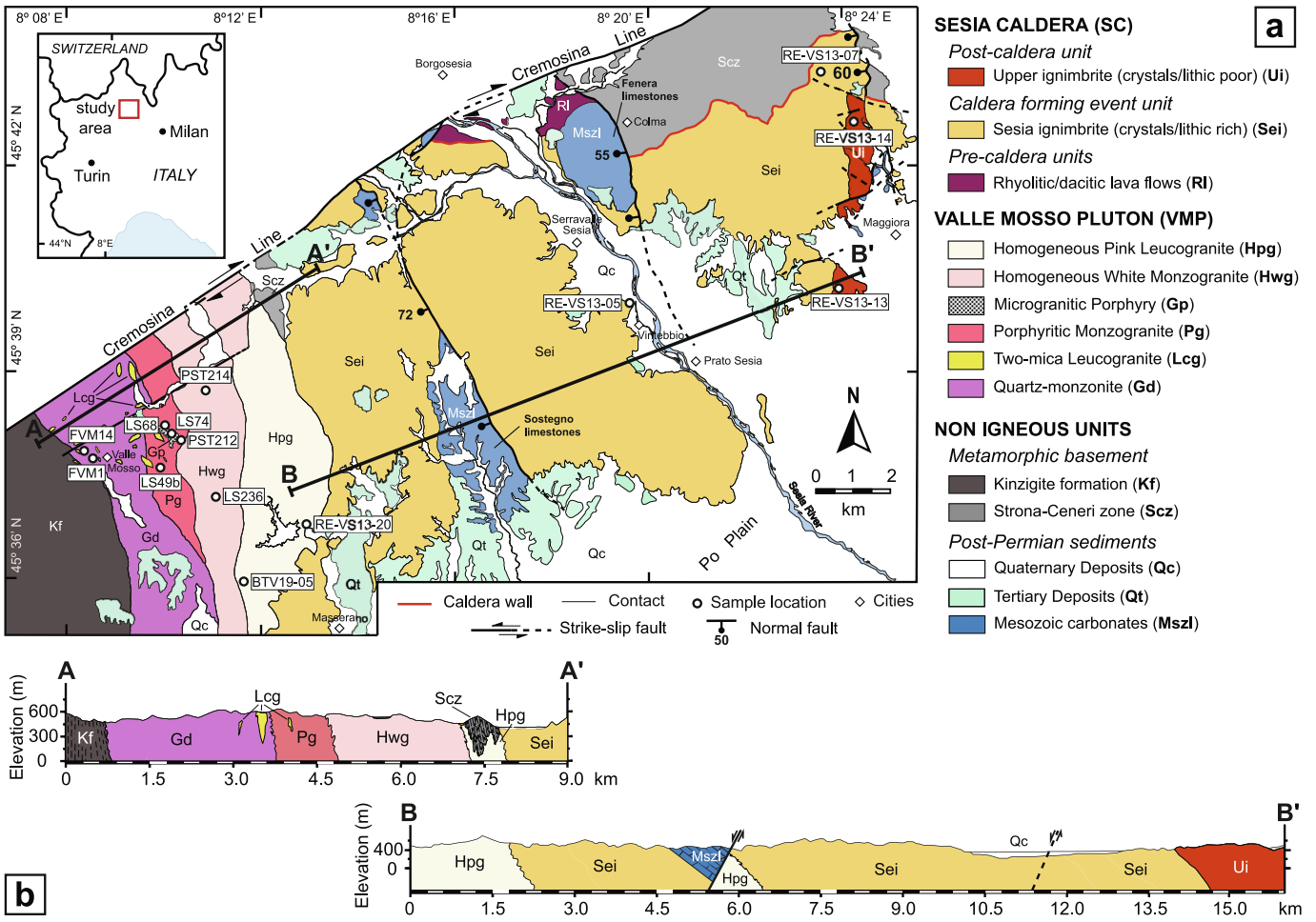

Fig. 1. (a) Detailed geological map of the Sesia Magmatic System south of the Cremosina line, including location of the sample analysed in this work. Modified after Sbisà (2009) and Tavazzani et al. (2020). (b) Cross-sections matching the geological map.

Table 1
List of samples selected for this study, including approximate distance from base of the intrusion calculated after Tavazzani et al. (2024).

Rock sample	Units	Label	Distance from intrusion's base (m)	Latitude (DD)	Longitude (DD)
RE-VS13–14	Upper Ignimbrite	*Ui*	–	45.712433°	8.408250°
RE-VS13–13	Upper Ignimbrite	*Ui*	–	45.675033°	8.400983°
RE-VS13–07	Sesia Ignimbrite	*Sei*	–	45.725000°	8.395278°
RE-VS13–05	Sesia Ignimbrite	*Sei*	–	45.670333°	8.332367°
RE-VS3–20	Homogeneous Pink Leucogranite	*Hpg*	7762	45.613142°	8.222232°
BTV19–05	Homogeneous Pink Leucogranite	*Hpg*	6050	45.600433°	8.197148°
PST214	Homogeneous White Monzogranite	*Hwg*	5090	45.645794°	8.182607°
LS236	Homogeneous White Monzogranite	*Hwg*	4999	45.620091°	8.190199°
PST212	Porphyritic Monzogranite	*Pg*	3996	45.634507°	8.174601°
LS74	Microgranitic Porphyry	*Gp*	3931	45.636117°	8.173365°
LS68	Microgranitic Porphyry	*Gp*	3778	45.638234°	8.171014°
LS49b	Porphyritic Monzogranite	*Pg*	3381	45.629726°	8.169582°
FVM1	Quartz-monzonite	*Gd*	584	45.635079°	8.137709°
FVM14	Quartz-monzonite	*Gd*	0	45.637611°	8.130583°

(Sinigoi et al., 2016; Tavazzani et al., 2020, 2024). Recent high precision Chemical Abrasion-Isotope Dilution- Thermal Ionization Mass Spectrometry (CA-ID-TIMS) zircon U-Pb studies on samples from the VMP (Karakas et al., 2019; Tavazzani et al., 2023) have shown that zircon crystallization in the different units was coeval over a ~ 1 Ma interval between 283.98 ± 0.06 and 282.97 ± 0.17 Ma (2σ uncertainty).

2.3. Sesia Caldera

The volcanic rocks outcropping along the Sesia Valley predominantly consist of crystal-rich rhyolite, encompassing a variety of structures such as lava flows, massive porphyries, ignimbrites, fragment-rich tuff intermixed with volcanic megabreccia (Sbisà, 2009). The distribution of megabreccia indicates that the minimum northeast-southwest caldera dimension exceeded 13 km (Quick et al., 2009). The main eruptive unit (Sesia ignimbrite; Sei) of the Sesia Caldera comprises densely welded crystal-rich (25–35 vol%) and lithic-rich (variable but up to 30 vol%) rhyolitic ignimbrites, containing patches of megabreccia (Fig. 1a). Textural and compositional attributes of quartz phenocrysts bear evidence of thermal rejuvenation of an evolved magma

body, stored at near-solidus high crystallinity conditions, which triggered the eruption of voluminous crystal-rich material (Tavazzani et al., 2020). Towards the eastern border of the volcanic field, the Sesia ignimbrite is covered by a crystal-poor (10–15 vol%) ignimbrite approximately 400 m thick (Upper ignimbrite; Ui). A layer of volcaniclastic sediments separates the two eruptive units. The Upper Ignimbrite unit is characterised by its high bulk rock silica content (75–77 wt% SiO_2), diffuse subparallel eutaxitic texture, small quartz phenocrysts (grain size 0.2–0.5 cm), and a general lack of lithic fragments. This unit has been interpreted as the outcome of a post-caldera eruptive event (Sbisà, 2009).

Recent high-precision CA-ID-TIMS, U-Pb age determinations on single zircons grains from the caldera-fill ignimbrite span from 284.61 ± 0.09 Ma to 283.37 ± 0.14 Ma (Karakas et al., 2019). Additionally, high-precision zircon CA-ID-TIMS ages from one samples of the post-caldera, Upper Ignimbrite unit (Tavazzani et al., 2023) indicate zircon crystallization between 283.53 ± 0.04 Ma and 283.22 ± 0.07 Ma. Eruption ages for both eruptions have been calculated either as Th-corrected $^{206}Pb/^{238}U$ ages derived from the youngest zircon within each eruptive unit (Sei: 283.46 ± 0.14/0.16/0.35 Ma; Ui: 283.22 ± 0.07/0.11/0.33 Ma) or as Bayesian estimates utilizing bootstrapped zircon distributions (Keller et al., 2018) as 283.49 ± 0.10/0.13/0.34 Ma for the Sesia Ignimbrite and 283.21 ± 0.10/0.13/0.34 Ma for the Upper Ignimbrite (Tavazzani et al., 2023). The eruption ages determined with either approach indicate a time interval of about 300,000 years between the two eruptive events.

3. Materials and methods

3.1. Samples

We investigated a total of 14 rock specimens, which include two samples for each intrusive and volcanic unit. The VMP granitic samples were selected to provide an idealized floor-to-roof section across the intrusion. In the lower part of the intrusion, we selected six samples: two from the quartz-monzonite unit (FVM14 and FVM1), two from the porphyritic monzogranite unit (LS49b and PST212), and two from the microgranitic porphyry unit (LS68 and LS74). In the upper portion, we selected two samples from the white monzogranite unit (PST214 and LS236) and two from the pink leucogranite unit (RE-VS13–20 and BTV19–05). Among the Sesia Caldera volcanic products, two samples represent the caldera-fill crystal-rich ignimbrites (Sesia Ignimbrite; RE VS13–05 and RE VS13–07) and two the late crystal-poor ignimbrite (Upper Ignimbrite; RE VS13–13 and RE VS13–14). Locations of samples studied in this work are shown in Fig. 1a and listed in Table 1, including the approximate distance from the floor of the intrusion for VMP granitic samples.

3.2. FTIR spectroscopy and OH-defects method

A total of 120 oriented quartz wafers were prepared for IR spectroscopy following the methodology outlined by Stalder and Konzett (2012). For every VMP granitic samples we prepared 10 crystals per sample (a total of 100 wafers). As for the SC volcanic products, five crystals per sample were studied (20 in total). The ten VMP granitic rock specimens were initially crushed mechanically; then, the fraction >250 μm was separated through sieving. Concerning the four SC volcanic samples, rock fragments were crushed in an agate mortar and individual euhedral quartz grains were handpicked from the crushed remnants. These quartz grains underwent a cleaning process involving a 10-min ultrasonic treatment with 3 X deionized H_2O, 1 × 1 N HNO_3 and 1 × 3 N HCl to remove any coatings formed by secondary alteration minerals.

Individual quartz crystals were handpicked under a microscope and oriented parallel to the optical axis in a thermoplastic resin on a glass slide. The alignment of crystals was verified using an optical microscope, confirmed by birefringence values of Δn = 0.009 under orthoscopic observation and by "flash figure" in conoscopic illumination. Subsequently, the samples were manually ground and polished on both sides while still in the resin. The thickness of each crystal was measured using a mechanical Mitutoyo micrometre gauge with an accuracy of ±2 μm. The thicknesses of crystals within the sample set range from 84 to 517 μm.

Polarized IR-spectroscopy on oriented crystals has been proven to be a valuable method to investigate OH-defects content and speciation in quartz (Stalder and Konzett, 2012). This technique enables the differentiation between molecular water (H_2O), which generates a broad absorption band ranging from 3000 to 3700 cm^{-1}, and water attributable to OH-defects, which produces distinct absorption peaks at specific wavenumbers, typically between 3250 and 3600 cm^{-1} (Kats, 1962). Since molecular water exhibits isotropic behaviour, while the majority of OH-defect absorption bands are more or less perfectly oriented perpendicular to the optical axis ($E\|n_o$), it becomes feasible to discern between these absorption features. Polarized measurements $E\|n_o$ capture both OH-defect and molecular water contributions, whereas measurements $E\|n_e$ solely detect molecular water. Consequently, the contribution of OH-defect can be determined by the subtraction as $E\|n_o - E\|n_e$ (Stalder and Konzett, 2012). The only OH dipole vector significantly contributing to $\|n_e$ measurements is associated with the B-related defect at 3595 cm^{-1}. To compute the absorption intensity A, the formula $A = \left(\frac{2\,n_o+n_e}{2}\right)$ is therefore employed (Stalder and Neuser, 2013; Stalder, 2021).

Infrared spectra were acquired at the Department of Geosciences of the Swedish Museum of Natural History in Stockholm at room temperature, using a Bruker Vertex 70 spectrometer equipped with a halogen-lamp source and a CaF_2 beam-splitter coupled to a Hyperion 2000 microscope with a ZnSe wire-grid polarizer and a nitrogen-cooled InSb detector. Between 200 and 400 scans were conducted for both background and sample, with a resolution of 4 cm^{-1} within the wavenumber range of 2000–5000 cm^{-1}. On each crystal, a visually inclusion-free volume was analysed with two measurements on the same spot (one $E\|n_o$ and one $E\|n_e$), the polarizer being rotated by 90° after the first measurement. The two polarized ($E\|n_o$ and $E\|n_e$) IR spectra obtained were then subtracted according to Stalder and Konzett (2012), baseline-corrected using a linear baseline within the wavenumber range 3600–3200 cm^{-1} via PeakFit® 4.12 environment and subsequently normalized to thickness. Determining the water content involves utilizing general calibration curves in accordance with the Beer-Lambert law. The absorption molar coefficient ε is estimated though different calibration methods. In this study, the mineral-specific calibration developed by Thomas et al. (2009) was used, i.e. $\varepsilon = 89\,000 \pm 15\,000$ L mol^{-1} cm^{-2}. The water content can accordingly be calculated as follows:

$$c\,(ppm\,H_2O) = \frac{A}{t} \bullet \frac{2 \bullet M_{H_2O} \bullet 1000}{D_{qz} \bullet 89000} = \frac{A}{t} \bullet 0.153 \quad (1)$$

with the molar mass of water $M_{H_2O} = 18\,g/mol$, the density of quartz $D_{qz} = 2.65\,g/cm^3$, and the thickness t in centimetres. The factor 2 represents the twofold contributions of n_o (out of the three spatial directions), and the factor 1000 is obtained from the conversion of litres to cubic centimetres (Stalder, 2021). Results are expressed as ppm H_2O weight notation (Supplementary Data Table S2).

The precision of the OH content determination is assessed to be approximately ±10 % when considering the main error sources, such as background correction, thickness measurement, and potential mismatch in crystal orientation (Stalder et al., 2017). Furthermore, a systematic uncertainty stemming from the limited accuracy of the extinction coefficient is estimated to be ±15–20 % (Libowitzky and Rossman, 1997; Thomas et al., 2009). The limit of detection heavily relies on spectra quality and sample thickness, and it can be estimated "visibly" as a peak

signal that surpasses the noise level twofold. For the analysed samples, a detection limit of 0.1 ppm weight H_2O has been approximated for spectra exhibiting the lowest noise levels.

3.3. LA-ICP-MS trace element analysis

Following FTIR spectroscopy, LA-ICP-MS analyses were conducted on the same quartz wafers. The quartz crystals were freed from the thermoplastic resin by rinsing the glass plate with acetone. Afterwards, the crystals were embedded in four circular 1 inch epoxy mounts, then ground and polished. To ensure that results of FTIR analyses are directly linked to LA-ICP-MS values, we analysed the same-inclusion-free volume targeted for IR-spectra acquisition. Moreover, we routinely placed a further LA-ICP-MS analytical spot at least 50 μm away from the initial one, to test for compositional homogeneity of the quartz grain. Trace elements concentrations in quartz were determined using a GeoLas system equipped with a Compex Pro 102F (Coherent) Excimer 193 nm (ArF) laser source coupled with a Nexion2000 (Perkin Elmer) fast-scanning quadrupole ICP-MS, housed at the Institute of Geochemistry and Petrology, ETH Zürich. The on-sample energy density of the laser beam was set at ca. 20 J•cm^{-2} with a repetition rate of 10 Hz. Quartz crystals were ablated with a spot size of 40 μm. The ablation was performed in an in-house cell designed for 1 inch mounts (Günther et al., 1997), using ca. 1.0 L•min^{-1} He as carrier gas flow and ca. 1.0 L•min^{-1} Ar make-up gas admixed downstream of the ablation chamber and homogenized through a squid device. The analysed set of elements is ^{7}Li, ^{9}Be, ^{11}B, ^{23}Na, ^{25}Mg, ^{27}Al, ^{39}K, ^{45}Sc, ^{49}Ti, ^{71}Ga, ^{72}Ge, ^{85}Rb, ^{88}Sr, and ^{133}Cs. Quantification for all elements was performed against the NIST SRM 610 glass, serving as the primary reference material (Jochum et al., 2011). For quartz analyses, a natural quartz crystal characterised by Audétat et al. (2015) was utilized as a secondary reference material. The average 2σ reproducibility of concentrations in the secondary quartz reference material across all analytical sessions was approximately 5 % relative. The raw data were processed using SILLS (Signal Integration for Laboratory Laser Systems) software package, developed in MATLAB® and specifically designed for reducing data and calculating elemental concentrations from transient LA-ICP-MS signals (Guillong et al., 2008). Silicon was used as internal standard for quartz (stoichiometric value). During the data reduction phase, analytical uncertainties and limits of detection were automatically computed for each element and each crystal (Supplementary Data Table S3).

In addition to quartz, selected trace element contents of feldspars were analysed using a 193-nm Resonetics ArF excimer laser coupled with a Thermo Element XR inductively coupled plasma mass spectrometer (LA-ICP-MS) with operation parameters following Cortes-Calderon et al. (2024) and detailed in Supplementary Material S1. The full set of results is available in Supplementary Data Table S4.

4. Results

4.1. OH-defect content and speciation

All 120 examined quartz crystals display at least one identifiable absorption peak associated with OH-defects (Fig. 2). In general, the dominant absorption feature for both VMP and SC quartz crystals is the Al-specific OH triplet at 3310, 3378, and 3430 cm^{-1}, which was detected in all analysed grains (Fig. 2). The Li-related substitution at 3480 cm^{-1} ranks as the second most prevalent, occurring in nearly all crystals. Exceptions are samples FVM14, FVM1, and RE-VS13–13, where only 1 out of 10, 7 out of 10, and 2 out of 5 crystals exhibited a Li-related absorption peak, respectively. The B-related defect at 3595 cm^{-1} is infrequent (11 crystals) and often challenging to identify due to the weakness of the absorption peak and the low signal-to-noise ratio in this region of the IR spectrum. The hydrogarnet defect (4H) at 3585 cm^{-1} is absent throughout all measurements. The acquired spectra show a notable prevalence of multiple substitutions (Al- and Li-related defects; Al- and B-related defects; Al-, Li- and B-related defects), with only 13 crystals exhibiting single substitutions (Al-related defects).

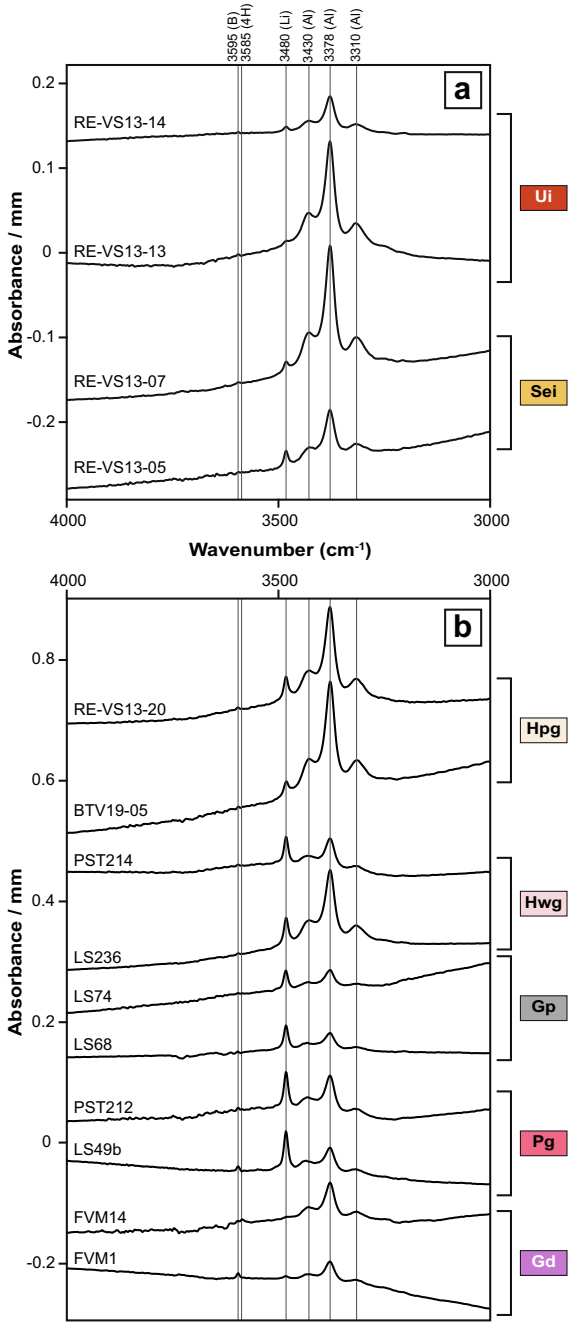

Fig. 2. Average IR spectra of (a) Sesia Caldera and (b) Valle Mosso Pluton samples in the OH spectral region. The spectra are normalized to quartz wafer thickness and offset vertically for clarity. Peaks position is marked with vertical grey lines. Refer to Table 1 for unit labels.

4.1.1. Valle Mosso Pluton

Average absorption spectra of VMP quartz crystals reveal a strong petrographic control on the variation in amount and type of OH-defects across the intrusion. Total OH water content increases with increasing distance from the base of the intrusion (Fig. 3a; Table 2). This trend also follows the degree of magmatic evolution: the basal quartz-monzonite is the least evolved unit within the VMP (67–72 wt% SiO_2; Tavazzani et al., 2020) and exhibits one of the lowest average OH content (3.6 ppm). Conversely, the leucogranite unit, which represents the most evolved

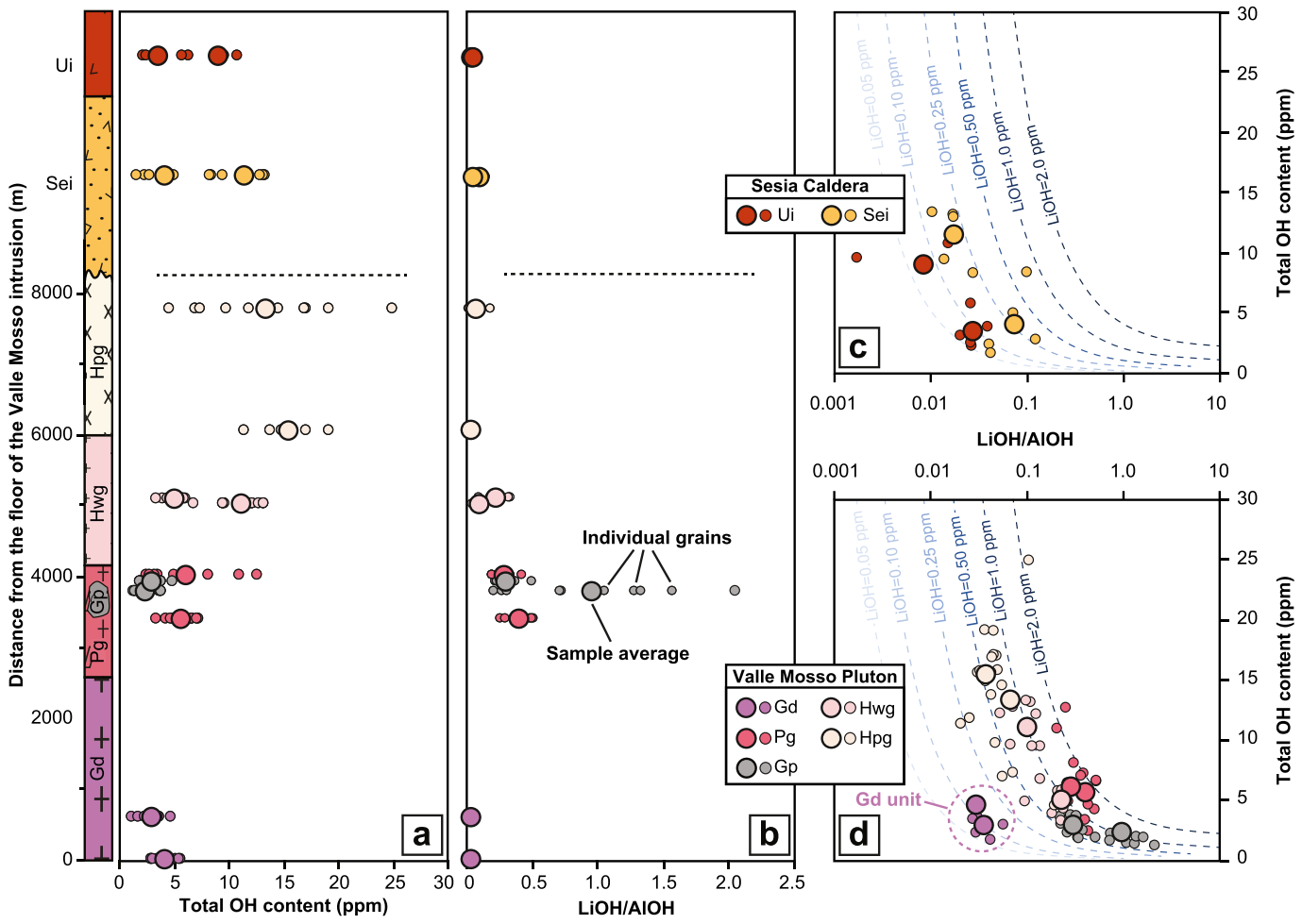

Fig. 3. (a) Variation in total OH water content for quartz grains across the Valle Mosso pluton (VMP) and the Sesia Caldera (SC) volcanic units. Uncertainty (1σ) on individual measurements is estimated to be between 10 and 20 % of the reported values (Libowitzky and Rossman, 1997; Thomas et al., 2009). (b) Variation in LiOH/AlOH ratio (derived from I_{3480}/I_{3378} band ratio) for the granitic and volcanic quartz crystals versus distance from the base of the intrusion and in the volcanic pile. Covariation of total LiOH/AlOH ratio with total OH water content for (c) SC and (d) VMP samples. Dashed lines represent theoretical trends for constant LiOH (0.05/0.10/0.25/0.50/1.0/2.0 ppm) at increasing AlOH values. Refer to Table 1 for unit labels.

Table 2
Total OH water content: minimum and maximum content, average, and standard deviation for each intrusive (VMP) and volcanic (SC) sample. Single contributions of Al-, Li-, and B-related defects are also shown. Samples with only one crystal showing a recognizable B-related absorption peak are marked with an asterisk (*).

	Unit	Sample	Total OH content			Single defects OH contributions		
						Al-related	Li-related	B-related
			Range (ppm)	Average (ppm)	σ	Range (ppm)	Range (ppm)	Range (ppm)
Sesia Caldera	*Ui*	RE-VS13–14	2.3–5.8	3.5	1.3	2.2–5.7	0.10–0.14	–
		RE-VS13–13	6.5–11	9.0	1.4	6.4–11	0.10–0.16	–
	Sei	RE-VS13–07	8.4–13	12	2.1	8.1–13	0.13–0.22	–
		RE-VS13–05	1.7–8.5	4.1	2.5	1.6–7.7	0.10–0.74	–
	Hpg	RE-VS13–20	4.6–25	13	6.0	3.9–22	0.29–2.3	0.24 *
		BTV19–05	11–19	15	1.9	11–19	0.23–0.78	–
Valle Mosso Pluton	*Hwg*	PST214	3.4–6.1	5.1	0.89	2.8–4.8	0.43–1.5	–
		LS236	6.8–13	11	2.0	6.0–12	0.60–1.3	0.10 *
	Gp	LS74	1.9–4.8	3.0	0.94	1.3–3.9	0.48–0.93	–
		LS68	1.3–3.9	2.4	0.97	0.43–3.1	0.66–1.2	–
	Pg	PST212	2.5–13	6.2	3.3	1.8–10	0.72–2.5	–
		LS49b	3.4–7.3	5.7	1.2	2.5–5.3	0.97–2.3	0.19–0.28
	Gd	FVM1	1.1–4.8	3.0	0.98	1.0–4.5	0.10–0.15	0.10–0.22
		FVM14	2.9–5.6	4.2	1.0	2.9–5.6	0.14 *	0.10 *

intrusive unit (up to 76.5 wt% SiO_2; Tavazzani et al., 2020), shows the highest average OH content (14 ppm) and individual crystals with up to 22 ppm total OH (Table 2).

The gradual decrease in LiOH/AlOH (I_{3480}/I_{3378}; where LiOH and AlOH refer to Li- and Al-specific OH-defects) band ratio across the VMP units illustrates a consistent decrease in LiOH contribution as well as an increase in AlOH with increasing distance from the base of the intrusion. An exception is observed in the quartz-monzonite unit, where both LiOH

and AlOH contributions remain low (Fig. 3b, d). Overall, Li-specific OH-defects are strongly subordinate to Al-specific defects in equigranular granitic units of the Valle Mosso Pluton (i.e. Hwg and Hpg, LiOH/AlOH <0.1; Figs. 2, 3). The porphyritic units of the intrusion (i.e. Pg and Gp) also show dominant Al-specific defects, but to a smaller degree than the equigranular units (0.1 < LiOH/AlOH <1) and include one sample from the microgranitic porphyry unit (Gp), characterised by anomalously high LiOH/AlOH ratios (i.e. >1; Fig. 3b, d). In the basal quartz-monzonite unit, both analysed samples display the lowest average LiOH content within the VMP dataset (0.12 ppm; Table 2), only one crystal in FVM14 and seven out of ten crystals in FVM1 exhibit recognizable Li-related absorption peaks. BOH defects are infrequent, and their occurrence is unevenly distributed within the sample set, favouring samples closer to the base of the intrusion (i.e. quartz-monzonite unit). Here, individual samples show BOH values comparable to those of LiOH (Fig. 2b).

4.1.2. Sesia Caldera

In samples from volcanic units, average spectra also exhibit fluctuations in OH-defect contents (Fig. 3a; Table 2). However, identifying a consistent pattern is more complex. The contribution from Al-related defects is significantly higher in two samples (RE-VS13–07 from Sesia and RE-VS13–13 from Upper ignimbrites) compared to companion samples from the same units (RE-VS13–05 from Sesia and RE-VS13–14 from Upper ignimbrites). LiOH contribution is minimal, with less than 1 ppm observed in only a few quartz grains from the Upper Ignimbrite unit and BOH defects are entirely absent in quartz phenocrysts from the Sesia Caldera.

4.2. Trace elements content

Due to the selective incorporation of trace elements in quartz and their variable limits of detection by LA-ICP-MS, only specific elements are presented here (i.e. ^{7}Li, ^{11}B, ^{23}Na, ^{25}Mg, ^{27}Al, ^{39}K, ^{45}Sc, ^{49}Ti, ^{72}Ge, and ^{88}Sr), all other elements are reported in Supplementary Data Table S3. Out of the relevant elements, Ti, Al, and Li are uniformly detected in all analysed quartz crystals, while elements such as Ge, Sr, Mg, and B are the least frequent (Table 3).

4.2.1. Valle Mosso Pluton

In quartz grains from the Valle Mosso granitic body, Al contents range from 40 to 202 ppm. At the base of the intrusion, quartz crystals exhibit the lowest Al content (40–143 ppm) (Fig. 4b). Moving upward into the overlying porphyritic monzogranite unit, Al content sharply increases before stabilizing across the intrusion in a range between 100 and 120 ppm (Table 3), with outliers potentially related to accidental breaching of small, undetected melt inclusion during quartz ablation. Throughout the lower part of the intrusion, Ti remains relatively constant, with average concentrations between 29 and 33 ppm. The units showing highest Ti contents (up to 100 ppm; Table 3) are the porphyritic monzogranite and microgranite porphyry units. Titanium content then decreases across the progressively more evolved equigranular monzogranite and leucogranite units (Table 3; Fig. 4c). It is to be noted that Ti concentration in quartz grains from both intrusive and volcanic lithologies can show substantial (i.e. 10s of ppm) variations at spatial scales not resolvable by LA-ICP-MS analyses (Tavazzani et al., 2020). This might add to the large scatter observed in Ti values across most units (Fig. 4b). The Li content is notably low in the basal quartz-monzonite unit (1.1–5.1 ppm), it sharply increases to 17–29 ppm in the porphyritic monzogranite and microgranite porphyry units, then tends to decrease with distance from the base of the intrusion, reaching 5.1–19 ppm in the high-silica leucogranite unit (Fig. 4a). Germanium concentration does not exhibit a discernible trend throughout the profile and remains close to the detection limit (~1 ppm).

4.2.2. Sesia Caldera

Within the volcanic products of the Sesia Caldera, the average Al content stands at 114 ppm in the Sesia Ignimbrite and 98 ppm in the Upper Ignimbrite (Fig. 4b). These volcanic units show the highest Ti content within the analysed quartz crystals, with an average of 37 ppm and 40 ppm for Sesia and Upper ignimbrites, respectively (Fig. 4c). Volcanic units of the Sesia Caldera display Li abundance in quartz that is roughly bimodal, with both units showing companion “high-Li” (20 ppm) and “low-Li” (13 ppm) samples (Fig. 4a). Germanium displays similar content across plutonic and volcanic unis (1.5 to 2.0 ppm) except for the Upper Ignimbrite samples whose Ge content is always below limit of detection.

5. Discussion

5.1. Control on quartz OH-defects and trace elements distribution in silicic systems

In the upper crustal, silicic portion of the Sesia Magmatic System, quartz trace element contents and OH-defects budget display systematic changes with their vertical position in the magmatic stratigraphy. In this section, we first identify the compositional characteristics of quartz crystals that are likely acquired during the supra-solidus crystallization history of the VMP and SC magmas, either in local equilibrium or disequilibrium with the surrounding melt and/or coexisting magmatic volatile phases. Following this assessment, we take into consideration the potential effect of post-crystallization processes (e.g. *syn*-eruptive and hydrothermal activity) that have been shown to impact both concentration of fast-diffusing trace elements (e.g. Li; Neukampf et al.,

Table 3
Trace element concentrations for each intrusive (VMP) and volcanic (SC) sample are reported as ranges; mean values are shown in parentheses. Samples with undeterminable range due to $n < 2$ values above the limit of detection are marked by an asterisk (*).

	Unit	Sample	Trace element concentrations (ppm)						
			Ti	Ge	Al	B	Li	Na	K
Sesia Caldera	*Ui*	RE-VS13–14	28–34 (30)	–	92–97 (95)	2.6–2.7 (2.7)	20–21 (21)	0.9–1.5 (1.2)	21–38 (31)
		RE-VS13–13	36–62 (50)	–	91–115 (101)	–	12–16 (14)	0.5–3.4 (1.8)	15–21 (18)
	Sei	RE-VS13–07	37–41 (38)	(1.2) *	94–204 (125)	2.5–3.4 (2.8)	11–14 (13)	0.4–5.0 (2.5)	14–79 (34)
		RE-VS13–05	35–40 (37)	(1.6) *	95–115 (103)	2.7–3.5 (3.0)	17–21 (20)	0.9–13 (4.8)	12–36 (24)
Valle Mosso Pluton	*Hpg*	RE-VS13–20	6–38 (19)	1.6–2.4 (2.0)	87–200 (125)	3.7–4.8 (4.1)	6.3–19 (13)	1.0–12 (5.5)	15–27 (22)
		BTV19–05	7–31 (20)	1.5–2.5 (1.9)	100–133 (110)	2.7–3.3 (3.0)	5.1–11 (8.2)	2.9–29 (10)	13–39 (23)
	Hwg	PST214	14–38 (26)	1.2–2.6 (1.9)	91–135 (117)	2.1–2.8 (2.4)	16–25 (21)	1.4–54 (14)	14–24 (19)
		LS236	18–51 (31)	1.7–2.4 (2.1)	89–177 (121)	2.0–4.3 (2.7)	12–24 (17)	0.8–33 (8.1)	15–28 (20)
	Gp	LS74	19–98 (37)	1.3–2.5 (1.9)	89–202 (112)	2.9–15.1 (6.1)	17–25 (21)	1.3–57 (11)	6.9–34 (19)
		LS68	15–41 (29)	1.5–1.7 (1.6)	87–139 (111)	1.3–3.3 (2.7)	18–26 (22)	0.7–14 (4.9)	4.4–11 (6.6)
	Pg	PST212	17–58 (33)	1.8–2.2 (2.0)	90–131 (107)	2.6–4.4 (3.0)	19–26 (22)	1.0–16 (4.4)	10–28 (16)
		LS49b	17–38 (25)	1.6–1.6 (1.6)	106–185 (131)	2.1–6.2 (3.3)	20–29 (23)	1.2–6.2 (3.5)	5.5–48 (17)
	Gd	FVM1	25–42 (32)	1.7–2.0 (1.9)	44–143 (76)	1.9–2.3 (2.2)	2.5–5.1 (4.1)	1.6–15 (8.5)	6.0–44 (22)
		FVM14	20–48 (32)	1.8–2.3 (2.1)	40–98 (53)	2.0–3.9 (3.1)	1.1–2.4 (1.8)	3.9–35 (13)	12–31 (20)

2022) and budget of interstitial OH-defects in quartz (e.g. LiOH; Suzuki and Nakashima, 1999; Frigo et al., 2016; Biró et al., 2017; Stalder et al., 2017). Throughout these sections we sidestep discussing trace elements and OH-defects result from quartz grains of the basal unit of the Valle Mosso Pluton (i.e. quartz-monzonite unit) as they are not conforming with general compositional trends.

5.1.1. Sensors for igneous processes (Al, Ge, Ti, AlOH)

Slow diffusing elements (e.g. Al, Ge, Ti; Cherniak et al., 2007; Tailby et al., 2018; Jollands et al., 2020b; Audétat et al., 2021) and lattice-bound OH-compounds (i.e. AlOH) display gradual, coherent trends across the Valle Mosso intrusion and Sesia volcanic units. The observed rather constant Al and Ge contents across all magmatic units (Fig. 4b) suggest that alumina excess (ASI; Shand, 1943) and degree of differentiation were nearly constant during crystallization. Indeed, all analysed units are granitic/rhyolitic, with only slight compositional changes between low- and high-silica compositions and all are peraluminous ($1.0 < ASI < 1.5$; Tavazzani et al., 2020). The upward decrease in Ti concentration, controlled by temperature and titanium activity (a_{TiO_2}) (Wark and Watson, 2006; Thomas et al., 2010; Huang and Audétat, 2012, among others), reflects crystallization from progressively more evolved melt batches. This trend is consistent with observations from other magmatic systems (e.g. Jacamon and Larsen, 2009) and suggests quartz crystallization from cooler and slightly more evolved magma. The higher average Ti values measured in volcanic units compared to their intrusive counterparts might reflect differences in the crystallization history of quartz grains between plutonic and volcanic environment (Suttner and Leininger, 1972; Fonseca Teixeira et al., 2024). Specifically, quartz grains that crystallize in plutonic environment will experience a wider range of temperatures, which span from quartz saturation to solidus (i.e. ~ 800 to 675 °C considering 2.5 wt% H_2O in the VMP granitic melt; Tavazzani et al., 2020, 2023) while quartz from eruptive products will stop crystallizing at temperatures that correspond to that of the eruption, necessarily supra-solidus (Fonseca Teixeira et al., 2024). Alternatively, the higher Ti values observed in volcanic units could be related to quartz grains recording pre-eruptive recharge by less evolved, hotter and/or higher a_{TiO_2} magmas (e.g. Wotzlaw et al., 2013; Szymanowski et al., 2017, 2019).

The ratios of slow diffusing elements (i.e. Al/Ti and Ge/Ti) in quartz grains from intrusive lithologies increase with distance from the base of the intrusion (5 to 25 for Al/Ti and 0.05 to 0.35 for Ge/Ti; Supplementary Fig. 1). This observation is also consistent with the increasing differentiation of magmatic units with stratigraphic height in the Valle Mosso Pluton (Tavazzani et al., 2020), a pattern observed in a number of different magmatic systems (e.g. Müller et al., 2005; Jacamon and Larsen, 2009; Breiter et al., 2013; Potrafke et al., 2020; Ji et al., 2024). In quartz grains from the Sesia Ignimbrite the Al/Ti and Ge/Ti ratios have average values of 2.8 and 0.03 respectively, which represent the lowest values observed in the entire dataset. This suggests that quartz phenocrysts in the rhyolite may have formed either (i) from a less evolved magma batch than that recorded in the Valle Mosso units, or (ii) from a hybrid (but still saturated in quartz) magma generated by the interaction of the granitic mush with a mafic recharge (see evidence for this in Tavazzani et al., 2020, 2023). Both scenarios are also consistent with the higher Ti values recorded in quartz grains from the Sesia volcanic units.

The gradual change in AlOH defects with distance from the base of the intrusion is not related to changes in abundance of elemental Al in quartz, which is nearly constant throughout the intrusive units (Fig. 5d). AlOH abundance shows instead complementary behaviour to Li content (Fig. 5c), which decreases with increasing distance from the base of the intrusion (from 30 to 10 ppm on average; Fig. 4a). This hints at the preferential formation of AlOH compared to dry AlLi defects as Li^+ competes with H^+ to charge-balance Al^{3+} (Fig. 6a). Considering H_2O as the dominant volatile phase (Tavazzani et al., 2024), an increase in water activity (a_{H_2O}) can explain progressively higher OH content (Fig. 6b; Stalder and Konzett, 2012; Frigo et al., 2016). This is particularly evident given the limited influence of melt temperature and composition on the formation of AlOH defects within the narrow

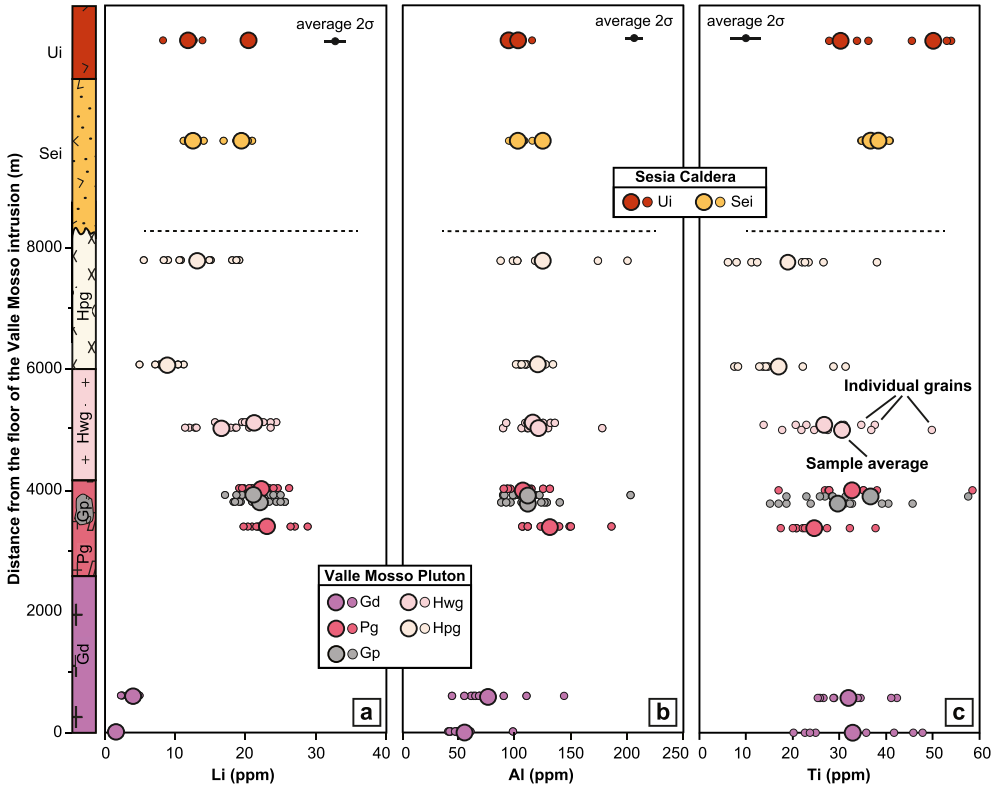

Fig. 4. Concentration of (a) Li, (b) Al, and (c) Ti for each intrusive (VMP) and volcanic (SC) sample. Average values for each sample are reported in Table 3. Refer to Table 1 for unit labels.

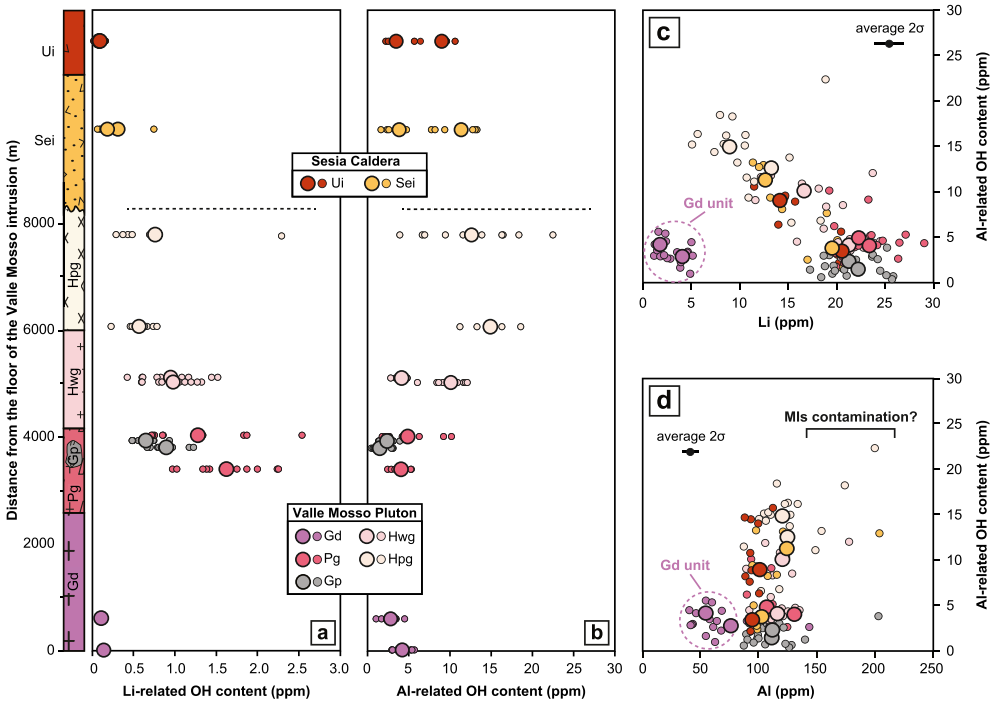

Fig. 5. Variation in (a) Li-related OH content and (b) Al-related OH content. Uncertainty (1σ) on individual measurements is estimated to be between 10 and 20 % of the reported values (Libowitzky and Rossman, 1997; Thomas et al., 2009). (c) Li concentration versus Al-related OH content and (d) Al concentration versus Al-related OH content. Refer to Table 1 for unit labels.

compositional range (68–75 wt% SiO_2) and temperature interval (~800–750 °C range of quartz saturation temperatures; Tavazzani et al., 2020) considered (Frigo et al., 2016). Increasing a_{H_2O} with progressive differentiation and shallower crystallization level of the granitic melts of the Valle Mosso pluton, which neared or reached saturation conditions for the high-silica leucogranite unit, is indicated by petrographic evidence (i.e. miarolitic cavities; Zezza, 1977; Tavazzani et al., 2017), thermodynamic and mass balance modelling (Tavazzani et al., 2024). This suggests that the average increase in AlOH in the Valle Mosso pluton likely reflects vertical changes in a_{H_2O} within an upper-crustal mush column, similarly to what observed by Potrafke et al. (2020) in a vertical transect of the Podlesí granite cupola. The comparative study of Müller and Koch-Müller (2009) also shows that lithologies formed in the magmatic environment but at high fluid activity (e.g. pegmatites) tend to have lower Al and higher AlOH compared to other igneous rocks (Fig. 6c, d). In this context, the larger scatter in AlOH values observed in quartz from the high-silica leucogranite unit might reflect juxtaposition of quartz grains recording water-undersaturated conditions vs. grains crystallized in a water-saturated environment.

The observed overlap in AlOH values between quartz grains from volcanic products of the Sesia Caldera and those from intrusive units (Fig. 5b) may be explained by two potential and non-mutually exclusive scenarios: (i) the heterogeneity could be inherited from different water saturation levels (cf. Frigo et al., 2016) in isolated pre-eruptive magma batches, later homogenized during the eruptive event (sensu Huber et al., 2009). Alternatively, (ii) the variable AlOH values might correspond to differential loss of Al-bound H^+ during eruption caused by sudden change in volatile activity (i.e. degassing, as observed by Jollands et al., 2020a; Neukampf et al., 2022). In this scenario, Li^+ would diffuse in the quartz rim to replace the lost H^+, forming dry AlLi defects (Jollands et al., 2020a, 2020c). However, since it is a spatially controlled process (diffusive exchange occurs in the near-rim area; Jollands et al., 2020a), further analyses specifically targeting the rim and core domains of the volcanic quartz crystals are required to confirm this hypothesis.

5.1.2. Sensors for cooling history and hydrothermal activity (Li, LiOH)

The initial Li distribution in quartz grains from intrusive units was likely controlled by the competition between Li^+ and H^+ for charge balancing Al^{3+} incorporation in the crystal structure during growth in the magmatic environment (see previous section; Figs. 5c, 6a, b). Similarly, higher concentration of Li in the melt (Frigo et al., 2016) or the interaction with a Li-rich magmatic volatile phase exsolved from the host magma (Tollan et al., 2019) would have favoured the formation of interstitial LiOH defects and dry AlLi defects over hydrous AlOH defects. However, given the mobility of Li and LiOH defects in the post-crystallization/hydrothermal environment, it is to be discussed whether their observed distribution patterns are inherited from magmatic processes or were modified by subsolidus processes. The mobility of elemental Li in and out of the quartz crystal lattice during eruptive events and in post-crystallization (e.g. hydrothermal) environment is well documented for quartz (Ellis et al., 2018; Jollands et al., 2020a; Neukampf et al., 2019, 2022). Similarly, thermal instability of interstitial LiOH defects during reheating and hydrothermal events has been experimentally demonstrated (Brunner et al., 1961; Rovetta et al., 1986; Kronenberg et al., 1986; Suzuki and Nakashima, 1999; Stalder et al., 2017).

The high diffusivity of elemental Li in quartz (Rottier et al., 2017; Jollands et al., 2020c, 2022) even at temperatures below the granitic solidus (i.e. for granitic melts of the VMP solidus is at ~675 °C; Tavazzani et al., 2020), would have driven Li-loss from quartz grains of slowly cooled units in the plutonic environment. The pattern of Li distribution in quartz across intrusive units can thus be interpreted as the result of differential cooling rates (Neukampf and Ellis, 2025). Indeed, timescale of cooling has been recognized as a crucial factor in Li preservation in pegmatitic bodies (Zhou et al., 2025), being a much more influential parameter than the initial Li concentration in the melt. This interpretation is reinforced by the distribution of the thermally unstable interstitial LiOH defect, which shows a direct correlation with elemental Li (Supplementary Fig. S2). The high LiOH/AlOH observed in the porphyritic units, and the dominance of LiOH in the microgranitic porphyry unit, which features textural (aphanitic matrix; Tavazzani

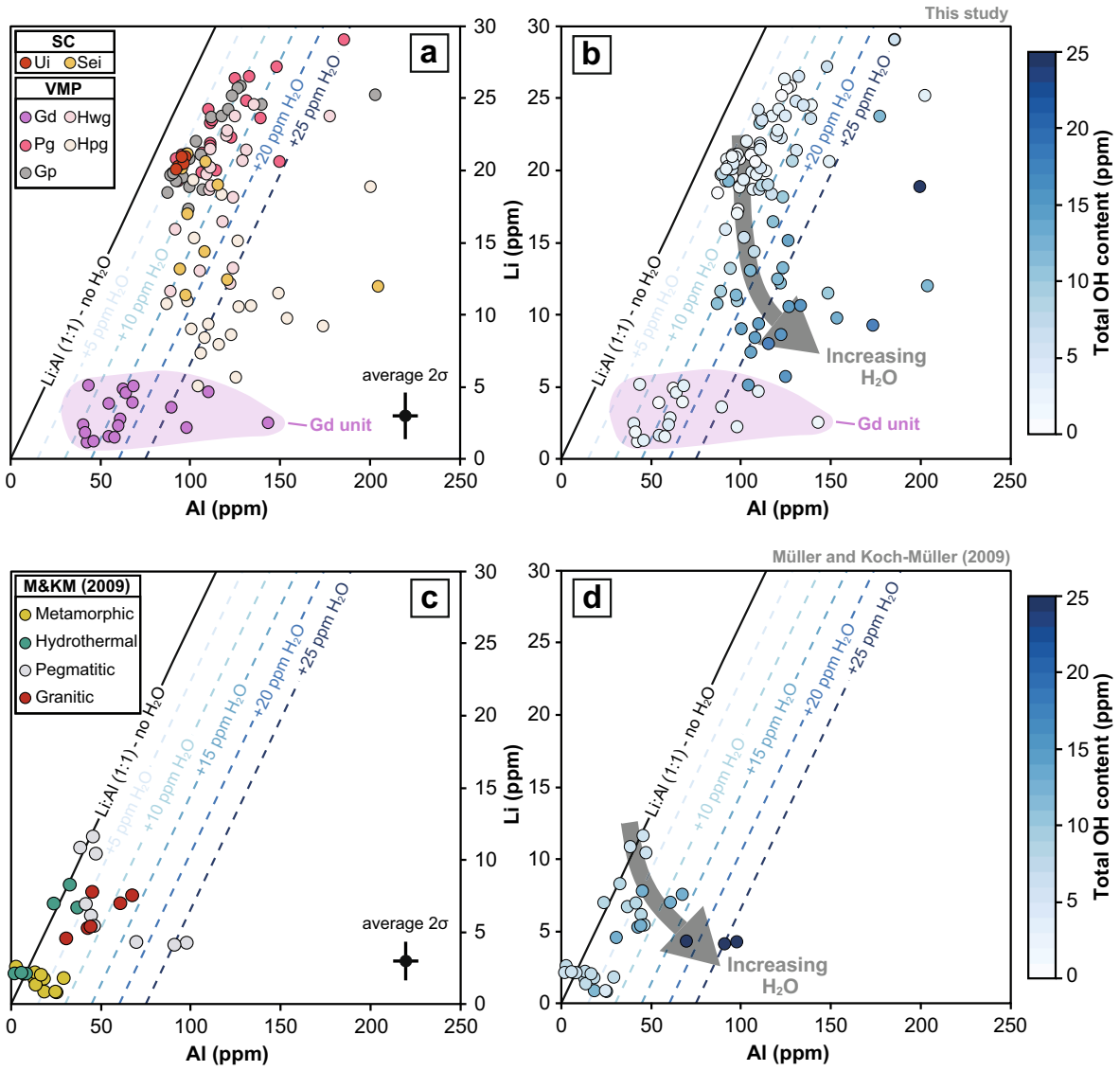

Fig. 6. Comparison of Al, Li and OH covariation between quartz grains from (a, b) the Sesia Magmatic System and (c, d) the study of Müller and Koch-Müller (2009). Samples are divided by units (a, c) and alternatively color-coded based on their total defect water content (b, d). Cationic exchange lines are from Neukampf et al. (2022). Refer to Table 1 for unit labels.

et al., 2017) and mineralogical (sharp Ti diffusional profiles; Tavazzani et al., 2020) evidence for quenching, suggest that LiOH defect distribution was mediated by cooling rate. Scenarios that would account for anomalously high Li incorporation or LiOH production in the magmatic environment are difficult to envision based on the available petrographic and geochemical data. Indeed, in the two units showing the highest Li and LiOH contents in quartz there is no indication of increased Li activity in the melt (Frigo et al., 2016) or the exsolution of a Li-rich volatile phase (Tollan et al., 2019). The concentration of Li measured in feldspars is unchanging across all intrusive units (Supplementary Fig. S3), regardless of degree of magmatic evolution, and there is no evidence of saturation of Li-bearing mineral phases (e.g. tourmaline) in the two units characterised by high Li and LiOH contents.

Although rapidly emplaced at the surface, the volcanic units might have also experienced prolonged post-eruptive cooling with potential Li loss (Ellis et al., 2018; Neukampf et al., 2022). As previously reported, Li loss might be differential depending on the position of the sample in the ignimbrite stratigraphy (Ellis et al., 2018). Samples collected from the welded basal vitrophyre horizon represent a magma batch quenched upon eruption, while samples gathered higher in the stratigraphy would have experienced prolonged thermal overprint during cooling and welding of the ignimbrite (Neukampf et al., 2022; Cortes-Calderon et al., 2024). Thus, samples that represent different stratigraphic horizons of the Sesia and Upper Ignimbrite units could reproduce the bimodality in elemental Li contents observed in this study (Fig. 4a). Unfortunately, the Sesia Caldera Ignimbrite is only outcropping in its intra-caldera facies and its internal structure was lost in the collapse of the caldera edifice (Quick et al., 2009). The stratigraphy of the Upper Ignimbrite is also poorly accessible due to the lack of continuative exposure of the unit (Sbisà, 2009). Therefore, testing the stratigraphic profile-related Li-loss hypothesis could be challenging even with a larger sample set.

Unlike elemental Li with its bimodal distribution, the lack of LiOH is ubiquitous in quartz grains from volcanic deposits as already observed in previous IR studies on volcanic quartz, which have revealed nearly exclusively Al-related OH-defects (Müller et al., 2009; Stalder and Neuser, 2013; Biró et al., 2016, 2017; Tollan et al., 2019; Hencz et al., 2021). This seemingly ubiquitous characteristic of volcanic quartz grains might be related to the irreversible decrease in LiOH bands under thermal or hydrothermal treatment (i.e. annealing; Brunner et al., 1961; Rovetta et al., 1986; Kronenberg et al., 1986; Suzuki and Nakashima, 1999; Stalder et al., 2017). This effect could have been caused both in the magmatic and post-crystallization environment through: (i) a short-

lived reheating episode (i.e. rejuvenation; Bachmann et al., 2005) that thoroughly affected the magma reservoir before eruption or, alternatively, (ii) the circulation of a hot (>300 °C; Stalder et al., 2017) fluid in the post-depositional environment. Pre-eruptive thermal rejuvenation of the magma reservoir is a possible pathway for the crystal-rich, Sesia Ignimbrite unit, which shows textural (e.g. phenocrysts corrosion) and mineralogical (e.g. inverse zoning) evidence for reheating (Tavazzani et al., 2020). However, samples collected from the smaller Upper Ignimbrite unit lack the textural and mineralogical disequilibrium features that would support injection of hotter, potentially less evolved magma in a rhyolitic mush, suggesting that another mechanism for destabilizing the interstitial LiOH defects was necessary. Mapping of alteration assemblages across eruptive products of the Sesia Caldera (Sbisà, 2009) shows that nearly the entire erupted volume of the Sesia Ignimbrite was affected by pervasive hydrothermal circulation. Fluid flow persisted even after the emplacement of the Upper Ignimbrite unit, which displays compositional and mineralogical modification related to weak/intermediate argillic alteration (Sbisà, 2009). Therefore, prolonged hydrothermal fluid circulation driven by the cooling Valle Mosso intrusion (hinted at by longer zircon crystallization timescales in intrusive units than in volcanic products; Tavazzani et al., 2023), could efficiently explain the barely detectable LiOH band in quartz from all volcanic units.

Overall, we demonstrated how the behaviour of slow-diffusing elements and lattice-bound OH compounds can record changes in intensive parameters of the magmatic system (e.g. temperature, a_{TiO_2}, a_{H_2O}) between quartz saturation and the solidus. Conversely, the distribution of fast-diffusing elements (e.g. Li) and non-lattice bound cations (e.g. H^+ associated to Li^+ in interstitial space) is irreversibly modified by the post-crystallization history of individual igneous units.

5.2. *Quartz grains from a silicic cumulate: inheritance or subsolidus modification?*

The basal quartz-monzonite unit of the Valle Mosso Pluton displays a markedly different signature from the overlying intrusive and volcanic units in terms of quartz trace elements distribution and OH inventory (Figs. 6, 7). This is evident not only in their deviation from the main compositional trends (Figs. 4, 5), but also in the anomalous values compared to the rest of the igneous system (Tables 2, 3). Hereafter we explore two non-mutually exclusive scenarios that could account for the extreme depletion in both slow-diffusing (e.g. Al, AlOH) and fast-

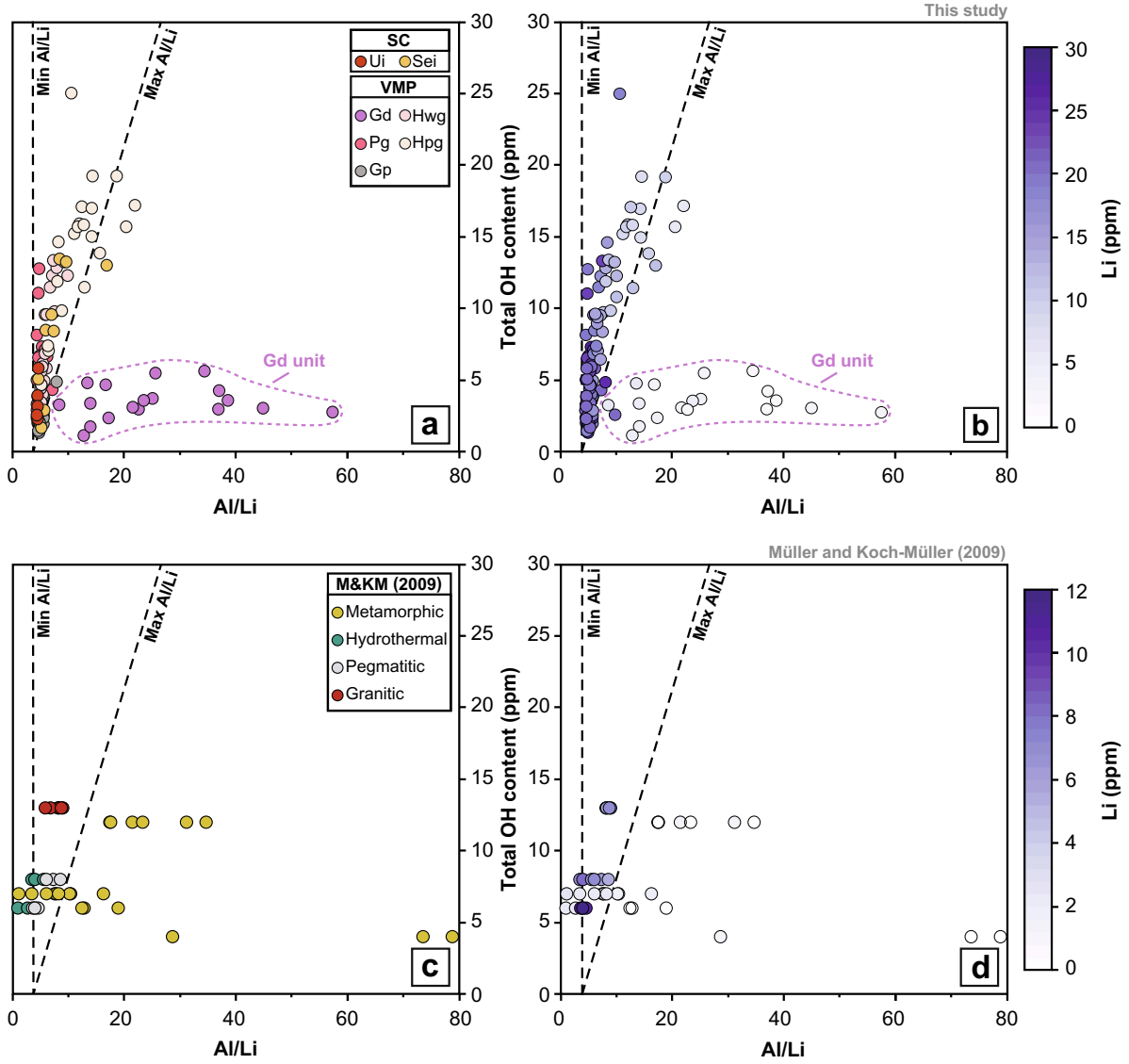

Fig. 7. Al/Li ratio covariation with total defect water content in quartz grains from (a, b) the Sesia Magmatic System and (c, d) the study of Müller and Koch-Müller (2009). Samples are divided by units (a, c) and color-coded based on their total Li content in ppm (b, d). Al/Li maximum and minimum lines are calculated by inverting the maximum OH level achievable by the cationic exchange formula of Müller and Koch-Müller (2009). Refer to Table 1 for unit labels.

diffusing (e.g. Li, LiOH) elements and hydrous defects in quartz grains from this unit, based on its petrologic context.

In previous studies (Tavazzani et al., 2020, 2024), rather than a product of in-situ magmatic crystallization, the basal quartz-monzonite unit has been interpreted as the cumulate residue leftover from fractional crystallization, which produced complementary high-silica melts now preserved as crystallized leucogranite in the Valle Mosso cupola. In this scenario, the incomplete extraction of haplogranitic residual melt from the cumulate unit (Tavazzani et al., 2024) would have left phenocrystic phases (e.g. quartz) in protracted contact (10^4–10^5 ka; Tavazzani et al., 2023) with an evolved, interstitial melt phase. The long residence at magmatic/sub-solidus temperature for this unit is suggested by the relaxed diffusion profiled of low diffusivity elements (e.g. Ti; Tavazzani et al., 2020). A process of partial recrystallization driven by the presence of a fluid phase exsolved from the evolved interstitial melt (i.e. through second-boiling) might have impacted the quartz grains from this unit (Troch et al., 2022). Indeed, the low Li concentration paired with high Na concentration observed in a number of quartz grains from this unit (Table 3) hint at quartz dissolution/recrystallization processes driven by interaction with a saline fluid (Larsen et al., 2004). During this process, Na^+ partitions into quartz whereas Li^+ preferentially partitions in the fluid phase, implying that Li^+ and Na^+ can partially migrate in and out of the quartz lattice during fluid-driven modifications (Larsen et al., 2004). Li^+ loss balanced by Na^+ incorporation could also explain the peculiar cation imbalance observed in Li-Al-H space (Fig. 6a, b). Presence of a detectable BOH band in quartz grains from the basal unit also hints at the presence of a hot, saline fluid interacting with quartz grains. This specific OH band is thermally stable up to 600 °C (Niimi et al., 1999), so its preservation would be ensured even if the quartz grains experienced a prolonged sub-solidus thermal history, conversely to the thermally unstable LiOH whose presence is negligible in quartz grains from this unit.

To explain the unique behaviour observed in quartz chemistry and defect inventory within the basal unit (Figs. 6, 7) an alternative mechanical process, unrelated to the petrologic or thermal history of the intrusion, could be called into action. Notably, certain trace element characteristics of quartz grains from the quartz-monzonite unit, such as depletion in Al, are problematic to explain through interaction with a fluid phase, due to the low diffusivity of Al through the quartz lattice (see Tailby et al., 2018). The quartz-monzonite unit shows evidence for entrainment of xenoliths of the metapelitic host-rock (Fig. 1; Tavazzani et al., 2017), either through stoping of m-sized blocks, erosion of cm-sized fragments or assimilation of individual crystals (i.e. garnet, also observed in other granitic bodies of the Sesia Magmatic System; Devoir et al., 2021). The quartz grains of this unit show unusually high Al/Li ratios (Figs. 6, 7) that are observed in other metapelitic sequences (Figs. 6c, d, 7c, d; Müller and Koch-Müller, 2009). This observation, coupled with the near-complete lack of LiOH defects – which are ubiquitous (if variable in amount) across all other igneous units – strongly hints at a metamorphic origin for quartz grains of the basal quartz-monzonite unit.

5.3. Trace elements and OH-defects in detrital quartz: a tool in provenance studies

In sedimentary petrology, the identification of siliciclastic material provenance is crucial for paleogeographic reconstructions (Haughton et al., 1991; Weltje and Von Eynatten, 2004). One of the most effective method is the study of chemistry (major and trace elements), age or isotopic composition of heavy mineral paragenesis via micro-beam analytical techniques (e.g. zircon, Lenaz et al., 2022; Spencer et al., 2024; tourmaline, Jafarzadeh et al., 2021; Lenaz et al., 2024; rutile, Triebold et al., 2012; Pereira and Storey, 2023; Cr-spinel, Lenaz et al., 2000; Kamenetsky et al., 2001; garnet, Mange and Morton, 2007; Lenaz et al., 2018). However, heavy minerals concentration can be both time-consuming and resource-intensive (Garzanti and Andò, 2007). Thus, weathering-resistant major rock-forming phases (e.g. quartz) have been proposed as an alternative valuable tool to fingerprint source rocks and tectonic environments in sedimentary sequences (e.g. Stalder and Neuser, 2013; Ackerson et al., 2015).

5.3.1. Trace elements-based discrimination diagrams

The use of quartz as source indicator in sedimentary petrology studies mainly focuses on the slow diffusing elements Al, (Ge), and Ti (e.g. Ackerson et al., 2015; Müller and Knies, 2013). Originally proposed by Schrön et al. (1988), a ternary diagram employing Ge – Ti – Al values has been used to categorize quartz from different types of granites, rhyolites, and pegmatites. A revised version of this classification plot was devised by Breiter et al. (2019) with new parameters (3*Ge – Ti – Al/10). Other authors tried to discriminate hydrothermal quartz from different ore settings based on Al/Ti, Sb/Ti, Ge/Ti, (Sb + Ge)/Ti, and Li/Al ratios (Rusk et al., 2008; Rottier and Casanova, 2021; Gao et al., 2022; Zhou et al., 2023). Zhang et al. (2022) proposed a bivariate Al vs. Ti diagram to discriminate quartz crystals from epithermal, skarn, Carlin-type Au, pegmatite-related, carbonatite-related and porphyry-type sources.

Our results indicate that slow-diffusing trace elements distribution can record the (re)crystallization environment of quartz at the scale of a single igneous system (see Section 5.1.1). However, we also find that relying on "global" compilations to accurately place quartz from unknown source to the correct provenance box remains problematic. Regarding the classification method of Zhang et al. (2022), samples analysed in this study fall within the "porphyry" field. While this represents an incorrect textural characterisation, it may still be a good estimation of the igneous nature of the Valle Mosso and Sesia Caldera quartz grains (Supplementary Fig. S4). Similarly, when applying the Ge-Ti-Al ternary diagram classification schemes of both Schrön et al. (1988) and Breiter et al. (2019), our samples plot in the "pegmatite" field (Supplementary Fig. S4), which does not exactly represent the source of quartz grains analysed in this study, but still indicate a shallow, evolved and volatile-rich magmatic environment. These observations suggest caution in using classification diagrams as a tool to assign a source lithology to a more detailed degree than igneous or non-igneous. An alternative approach, potentially involving machine learning like those proposed by Wang et al. (2021) and Saha et al. (2024), could be more effective by considering a larger number of variables into the analysis.

5.3.2. OH-defects as a provenance tool

In the past decade, OH-defects method in detrital quartz have emerged as a valuable tool for provenance studies, thanks to its relatively fast, low-cost, and simple analytical protocol (Stalder, 2014; Stalder et al., 2017, 2019; Jaeger et al., 2019; Bernardi et al., 2022; Bernardi, 2024). A general threshold of 5 ppm water content has been proposed to distinguish quartz of broadly magmatic (>5 ppm) from non-magmatic (<5 ppm) origin (Stalder and Neuser, 2013), based on analyses of grains from NW Germany and reference spectra from known rock types (igneous, metamorphic, pegmatitic and hydrothermal). Beyond total water content, OH speciation provides additional constraints: Li related defects are preferentially incorporated in quartz identified as hydrothermal, while Al related defects tend to be more stable during metamorphic processes than B- and Li-related ones (Stalder and Konzett, 2012; Stalder and Neuser, 2013; Stalder, 2014). This approach has proven effective across different tectonic settings, including (i) fluvial and offshore sediments from subduction zones in Japan, where OH-defects were introduced as a provenance tool in active margins (Jaeger et al., 2019), and (ii) sandstones from synorogenic foreland basins in NE Italy, Slovenia, and Croatia, where variations in OH-defect inventories tracked changes in sediment supply (Bernardi et al., 2022; Bernardi, 2024).

As far as concern the OH-defects, our findings confirm that OH-defect contents in magmatic quartz are typically higher than 5 ppm. Samples with OH-defect contents below this threshold may be considered

borderline between magmatic and metamorphic origins. However, the large variability in speciation of OH defects observed in the Valle Mosso intrusion (Fig. 3d), which is related to the diverse post-crystallization histories of single intrusive units, indicate that the OH speciation criteria require a degree of caution. While the OH content appears promising as a tool, a larger number of studies focused on characterising in detail potential protoliths is needed to improve robustness.

6. Conclusions

Variations in quartz OH-defects and trace elements observed in the silicic units of the Sesia Magmatic System provide fresh insights into the magmatic and post-crystallization environments in volcanic-plutonic system (Fig. 8):

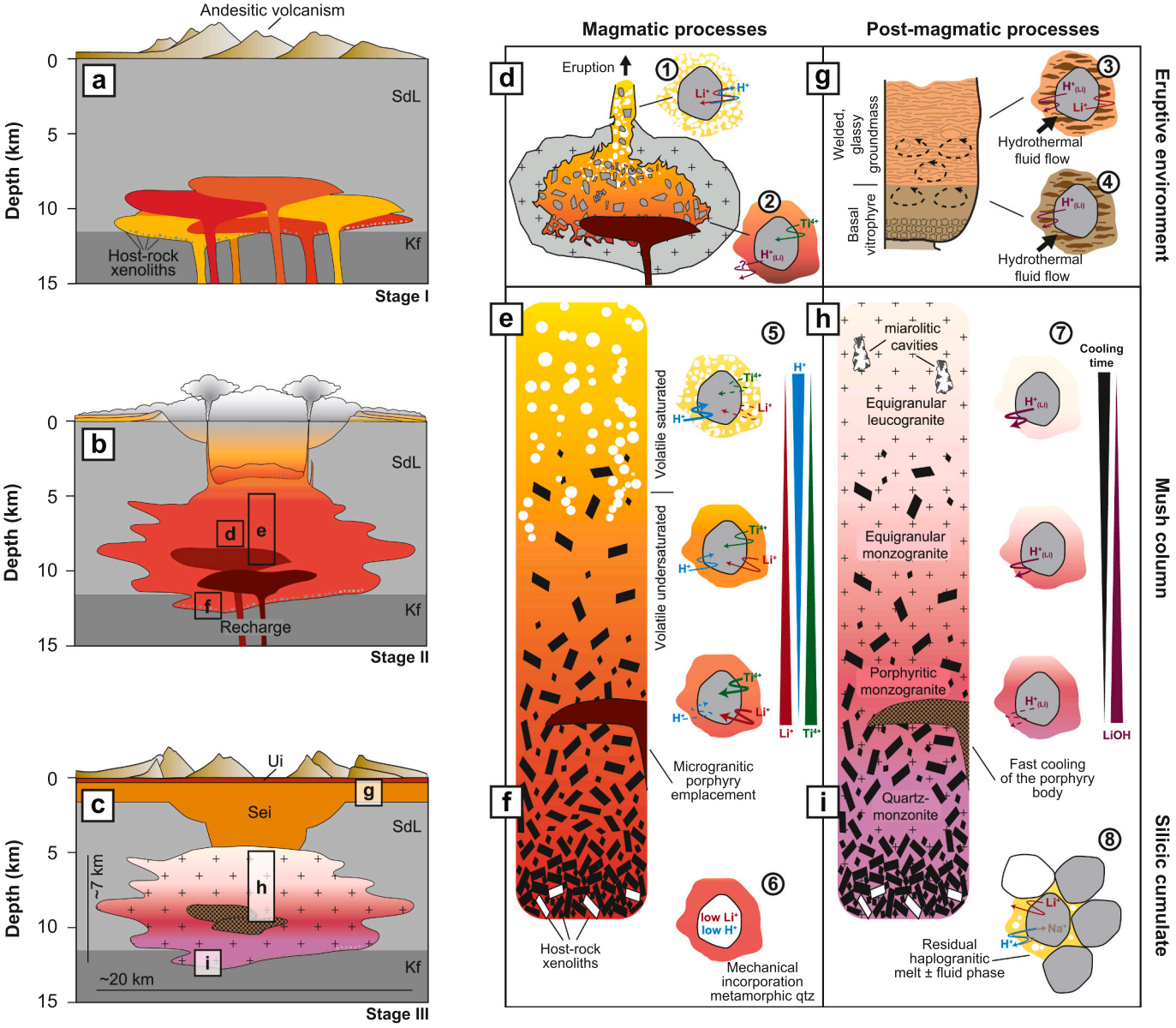

Fig. 8. The left-side panels portray a simplified view of the upper crustal evolution of the Sesia Magmatic System (SMS) from (a) incipient pluton construction, to (b) cataclysmic Sesia Caldera eruption, and finally (c) complete crystallization of the Valle Mosso pluton. The right-side panels illustrate the magmatic to post-magmatic history of quartz crystals at various levels of the SMS, from (d, g) the volcanic units (pre- and post-eruption) to (e, h) the Valle Mosso granitic intrusion (pre- and post-crystallization) and (f, i) its basal contact with metamorphic host-rock. Abbreviations used: Kf – Kinzigite Formation, SdL – Serie dei Laghi, Sei – Sesia Ignimbrite, Ui – Upper Ignimbrite. Specific magmatic to post-magmatic processes recorded in quartz OH inventory and geochemistry are highlighted: (1) Diffusional exchange of H^+ and Li^+ drives outward H^+ diffusion and inward Li^+ diffusion during open-system, disequilibrium degassing. (2) Influx of hotter magma in a crystal-rich mush promotes Ti^{4+} incorporation and outward diffusion of Li-related H^+. (3) Slow cooling in the central part of an ignimbrite flow unit causes diffusional loss of Li^+ while hydrothermal fluid flow destabilizes and provokes outward diffusion of Li-related H^+. (4) Quartz crystals from the fast-cooled basal vitrophyre retain their magmatic Li budget but still experience loss of Li-related H^+ due to hydrothermal fluid flow. (5) Varying degree of melt evolution and water activity across the Valle Mosso magma column define decreasing Li and Ti and increasing OH trend with height above the intrusion floor. (6) Mechanical incorporation of xenocrystic quartz grains from the metamorphic host rock near the intrusion floor. (7) Variation in cooling rate across units of the intrusion affects the loss of interstitial, Li-related H^+. (8) Presence of interstitial, haplogranitic melt phase in the basal, cumulate unit of the Valle Mosso pluton leads to disproportionate diffusional loss of Li^+ and H^+, likely balanced by Na^+ incorporation. Artwork is partially adapted from Forni et al. (2018), Ellis et al. (2022) and Neukampf et al. (2022).

- Slow diffusing elements (e.g. Al, Ge, Ti) and lattice-bound OH-compounds (i.e. AlOH) exhibit systematic variations across intrusive and volcanic units, except for the basal quartz-monzonite unit, which displays distinct behaviour (Fig. 8e, f).
- Increasing Al/Ti and Ge/Ti ratios in the Valle Mosso intrusion reflect increasing differentiation, while lower ratios in volcanic quartz suggest that erupted quartz phenocrysts may have formed either (i) from a less evolved magma batch, or (ii) from a hybrid magma generated by the interaction of the granitic mush with a mafic recharge.
- Al-related OH-defects increase with stratigraphic height in the intrusion, correlating with higher water activity during late-stage crystallization (Fig. 8e). AlOH abundance shows an inverse relationship with Li content, suggesting preferential formation of AlOH over dry AlLi defects. Quartz grains from the Sesia Caldera show AlOH values similar to the intrusive units but with significant variability, likely due to differences in pre-eruptive water saturation conditions or degassing-driven modifications (Fig. 8d).
- The distribution of thermally unstable LiOH defects, which directly correlates with elemental Li, suggests differential cooling rates across the *V*alle Mosso Pluton (Fig. 8h). In volcanic quartz, the bimodal Li distribution and ubiquitous, near-zero LiOH content, may be related to either *syn*-eruptive (recharge, degassing) or post-eruptive (variable cooling rates in the ignimbrite pile, hydrothermal alteration) processes (Fig. 8g).
- The basal quartz-monzonite unit of the Valle Mosso Pluton – which represent the cumulate residue leftover from fractional crystallization (Tavazzani et al., 2020) – shows trace element distributions consistent with either (i) prolonged contact with interstitial, evolved melt (Fig. 8i) or (ii) mechanical incorporation of quartz of metamorphic origin, supported by high Al/Li ratios, low LiOH, and evidence of host-rock assimilation (Fig. 8f).

Overall, slow-diffusing elements (Al, Ge, Ti) and AlOH defects preserve a magmatic signature, whereas fast-diffusing elements (Li) and LiOH defects record post-crystallization processes, which can significantly modify quartz in both trace element composition and OH-defect inventory. The combined analysis of these features in quartz can therefore offer a powerful tool for reconstructing the thermal and chemical evolution of magmatic systems, from magma chamber processes to post-eruptive alteration. As a corollary, findings of this study also confirm that slow-diffusing elements can help identify quartz crystallization environments, but classification diagrams may yield ambiguous results. Similarly, while OH-defect content appears promising, greater volume of studies is needed to enhance its reliability as a provenance tool.

CRediT authorship contribution statement

G. Tumaini: Investigation, Methodology, Formal analysis, Data curation, Writing – original draft. **L. Tavazzani:** Conceptualization, Investigation, Methodology, Formal analysis, Data curation, Writing – original draft. **H. Skogby:** Methodology, Validation, Writing – review & editing. **F. Bernardi:** Investigation, Formal analysis, Writing – review & editing. **S. Sinigoi:** Conceptualization, Writing – review & editing. **D. Lenaz:** Investigation, Resources, Supervision, Conceptualization, Writing – original draft.

Declaration of competing interest

The authors declare that they have no known competing financial interests or personal relationships that could have appeared to influence the work reported in this paper.

Acknowledgements

The authors would like to thank Julia Neukampf and Roland Stalder for their constructive and thoughtful reviews, which significantly improved the clarity and quality of the manuscript. The authors also thank Stefano Peres and Rita Economos for their help during sample collection and for stimulating discussions regarding the magmatism of the Sesia Magmatic System. Finally, the University of Trieste Erasmus+ Traineeship international mobility program is acknowledged for financial support.

Appendix A. Supplementary data

Supplementary data to this article can be found online at https://doi.org/10.1016/j.chemgeo.2025.122810.

Data availability

Data is provided with submission as Supplementary Tables.

References

Ackerson, M.R., Tailby, N.D., Watson, E.B., 2015. Trace elements in quartz shed light on sediment provenance. Geochem. Geophys. Geosyst. 16, 1894–1904. https://doi.org/10.1002/2015GC005896.

Aines, R.D., Rossman, G.R., 1984. Water in minerals? A peak in the infrared. J. Geophys. Res. 89, 4059–4071. https://doi.org/10.1029/JB089iB06p04059.

Audétat, A., 2013. Origin of Ti-rich rims in quartz phenocrysts from the Upper Bandelier Tuff and the Tunnel Spring Tuff, southwestern USA. Chem. Geol. 360–361, 99–104. https://doi.org/10.1016/j.chemgeo.2013.10.015.

Audétat, A., Garbe-Schönberg, D., Kronz, A., Pettke, T., Rusk, B., Donovan, J.J., Lowers, H.A., 2015. Characterisation of a natural quartz crystal as a reference material for microanalytical determination of Ti, Al, Li, Fe, Mn, Ga and Ge. Geostand. Geoanal. Res. 39, 171–184. https://doi.org/10.1111/j.1751-908X.2014.00309.x.

Audétat, A., Miyajima, N., Wiesner, D., Audinot, J.-N., 2021. Confirmation of slow Ti diffusion in quartz by diffusion coupleexperiments and evidence from natural samples. Geology. https://doi.org/10.1130/G48785.1.

Bachmann, O., Dungan, M.A., Bussy, F., 2005. Insights into shallow magmatic processes in large silicic magma bodies: the trace element record in the fish Canyon magma body, Colorado. Contrib. Mineral. Petrol. 149, 338–349. https://doi.org/10.1007/s00410-005-0653-z.

Bambauer, H.U., 1961. Spurenelementgehalte und γ-Farbzentren in Quartzen aus Zerrklüften der Schweizen Alpen. Schweiz. Mineral. Petrogr. Mitt. 41, 335–369.

Bambauer, H.U., Brunner, G.O., Laves, F., 1963. Merkmale des OH-Spektrums alpiner Quarze (3μ-Gebiet). Schweiz. Mineral. Petrogr. Mitt. 43, 259–268.

Baron, M.A., Stalder, R., Konzett, J., Hauzenberger, C.A., 2015. OH-point defects in quartz in B- and Li-bearing systems and their application to pegmatites. Phys. Chem. Miner. 42, 53–62. https://doi.org/10.1007/s00269-014-0699-4.

Bernardi, F., 2024. Quartz in Sedimentary Rocks: OH-Defects and Trace Elements for Provenance Studies. Ph.D. Thesis. University of Trieste, Trieste, Italy, p. 183.

Bernardi, F., Skogby, H., Lenaz, D., 2022. OH-defects in detrital quartz grains from the Julian Basin (NE Italy and Slovenia): a Fourier Transform infrared study. Geosciences 12, 90.

Beurlen, H., Müller, A., Silva, D., Da Silva, M.R.R., 2011. Petrogenetic significance of LA-ICP-MS trace-element data on quartz from the Borborema Pegmatite Province, Northeast Brazil. Mineral. Mag. 75, 2703–2719. https://doi.org/10.1180/minmag.2011.075.5.2703.

Biró, T., Kovács, I.J., Király, E., Falus, G., Karátson, D., Bendo, Z., Fancsik, T., Sándorné, J.K., 2016. Concentration of hydroxyl defects in quartz from various rhyolitic ignimbrite horizons: results from unpolarized micro-FTIR analyses on unoriented phenocryst fragments. Eur. J. Mineral. 28, 313–327. https://doi.org/10.1127/ejm/2016/0028-2515.

Biró, T., Kovács, I.J., Karátson, D., Stalder, R., Király, E., Falus, G., Fancsik, T., Sándorné, J.K., 2017. Evidence for post-depositional diffusional loss of hydrogen in quartz phenocryst fragments within ignimbrites. Am. Mineral. 102, 1187–1201. https://doi.org/10.2138/am-2017-5861.

Boriani, A., Burlini, L., Caironi, V., Giobbi Origoni, E., Sassi, A., Sesana, E., 1988. Geological and petrological studies on the hercynian plutonism of Serie Dei Laghi–geological map of its occurrence between Valsesia and Lago Maggiore (N-Italy). Rend. Soc. It. Mineral. Petrol. 43 (367), 84.

Botis, S.M., Pan, Y., 2009. Theoretical calculations of $[AlO_4/M^+]^0$ defects in quartz and crystal-chemical controls on the uptake of Al. Mineral. Mag. 73, 537–550. https://doi.org/10.1180/minmag.2009.073.4.537.

Breiter, K., Svojtka, M., Ackerman, L., Švecová, K., 2012. Trace element composition of quartz from the Variscan Altenberg–Teplice caldera (Krušné hory/Erzgebirge Mts, Czech Republic/Germany): insights into the volcano-plutonic complex evolution. Chem. Geol. 326–327, 36–50. https://doi.org/10.1016/j.chemgeo.2012.07.028.

Breiter, K., Ackerman, L., Svojtka, M., Müller, A., 2013. Behavior of trace elements in quartz from plutons of different geochemical signature: a case study from the Bohemian Massif, Czech Republic. Lithos 175–176, 54–67. https://doi.org/10.1016/j.lithos.2013.04.023.

Breiter, K., Lamarão, C.N., Borges, R.M.K., Dall'Agnol, R., 2014. Chemical characteristics of zircon from A-type granites and comparison to zircon of S-type granites. Lithos 192–195, 208–225. https://doi.org/10.1016/j.lithos.2014.02.004.

Breiter, K., Badanina, E., Ďurišová, J., Dosbaba, M., Syritso, L., 2019. Chemistry of quartz – a new insight into the origin of the Orlovka Ta-Li deposit, Eastern Transbaikalia, Russia. Lithos 348–349, 105206. https://doi.org/10.1016/j.lithos.2019.105206.

Breiter, K., Ďurišová, J., Dosbaba, M., 2020. Chemical signature of quartz from S- and A-type rare-metal granites – a summary. Ore Geol. Rev. 125, 103674. https://doi.org/10.1016/j.oregeorev.2020.103674.

Brunner, G.O., Wondratschek, H., Laves, F., 1961. Ultrarotuntersuchungen über den Einbau von H in natürlichem Quarz. Z. Elektrochem. 65, 735–750.

Cherniak, D.J., Watson, E.B., Wark, D.A., 2007. Ti diffusion in quartz. Chem. Geol. 236, 65–74. https://doi.org/10.1016/j.chemgeo.2006.09.001.

Connop, C.H., Smye, A.J., Garber, J.M., Moser, A.C., Caddick, M.J., Vervoort, J.D., 2024. Assembly of lower continental crust: a garnet Lu-Hf petrochronological investigation of the Ivrea-Verbano Zone, Italy. Earth Planet. Sci. Lett. 634, 118677. https://doi.org/10.1016/j.epsl.2024.118677.

Cortes-Calderon, E.A., Ellis, B.S., Magna, T., Tavazzani, L., Ulmer, P., 2024. Lithium systematics in the Krafla volcanic system: comparison between surface rhyolites and felsic cuttings from the Iceland deep drilling project −1 (IDDP-1). Contrib. Mineral. Petrol. 179, 37. https://doi.org/10.1007/s00410-024-02119-y.

Demarchi, G., Quick, J.E., Sinigoi, S., Mayer, A., 1998. Pressure gradient and original orientation of a lower-crustal intrusion in the Ivrea-Verbano Zone, Northern Italy. J. Geol. 106 (5), 609–622. https://doi.org/10.1086/516045.

Devoir, A., Bloch, E., Müntener, O., 2021. Residence time of igneous garnet in Si-rich magmatic systems: Insights from diffusion modeling of major and trace elements. Earth Planet. Sci. Lett. 560, 116771. https://doi.org/10.1016/j.epsl.2021.116771.

Drivenes, K., Larsen, R.B., Müller, A., Sørensen, B.E., 2016. Crystallization and uplift path of late Variscan granites evidenced by quartz chemistry and fluid inclusions: example from the Land's End granite, SW England. Lithos 252–253, 57–75. https://doi.org/10.1016/j.lithos.2016.02.011.

Ellis, B.S., Szymanowski, D., Magna, T., Neukampf, J., Dohmen, R., Bachmann, O., Ulmer, P., Guillong, M., 2018. Post-eruptive mobility of lithium in volcanic rocks. Nat. Commun. 9, 3228. https://doi.org/10.1038/s41467-018-05688-2.

Ellis, B.S., Szymanowski, D., Harris, C., Tollan, P.M.E., Neukampf, J., Guillong, M., Cortes-Calderon, E.A., Bachmann, O., 2022. Evaluating the potential of rhyolitic glass as a lithium source for brine deposits. Econ. Geol. 117, 91–105. https://doi.org/10.5382/econgeo.4866.

Fonseca Teixeira, L.M., Laurent, O., Troch, J., Siddoway, C.S., Tavazzani, L., Deering, C., Bachmann, O., 2024. Tracking quartz and zircon provenance in sedimentary rocks using Ti distributions: unlocking the volcanic-plutonic connection in old igneous systems. Earth Planet. Sci. Lett. 643, 118906. https://doi.org/10.1016/j.epsl.2024.118906.

Forni, F., Degruyter, W., Bachmann, O., De Astis, G., Mollo, S., 2018. Long-term magmatic evolution reveals the beginning of a new caldera cycle at Campi Flegrei. Sci. Adv. 4, eaat9401. https://doi.org/10.1126/sciadv.aat9401.

Fountain, D.M., 1976. The Ivrea-Verbano and Strona-Ceneri zones, Northern Italy: a cross-section of the continental crust—new evidence from seismic velocities of rock samples. Tectonophysics 33, 145–165. https://doi.org/10.1016/0040-1951(76)90054 -8.

Frigo, C., Stalder, R., Hauzenberger, C.A., 2016. OH defects in quartz in granitic systems doped with spodumene, tourmaline and/or apatite: experimental investigations at 5–20 kbar. Phys. Chem. Miner. 43, 717–729. https://doi.org/10.1007/s00269-016-0828-3.

Fu, S., Lan, Q., Yan, J., 2020. Trace element chemistry of hydrothermal quartz and its genetic significance: a case study from the Xikuangshan and Woxi giant Sb deposits in southern China. Ore Geol. Rev. 126, 103732. https://doi.org/10.1016/j.oregeorev.2020.103732.

Gao, S., Zou, X., Hofstra, A.H., Qin, K., Marsh, E.E., Bennett, M.M., Li, G., Jiang, J., Su, S., Zhao, J., Li, Z., 2022. Trace elements in quartz: insights into source and fluid evolution in magmatic-hydrothermal systems. Econ. Geol. 117, 1415–1428. https://doi.org/10.5382/econgeo.4943.

Garate-Olave, I., Müller, A., Roda-Robles, E., Gil-Crespo, P.P., Pesquera, A., 2017. Extreme fractionation in a granite–pegmatite system documented by quartz chemistry: the case study of Tres Arroyos (Central Iberian Zone, Spain). Lithos 286–287, 162–174. https://doi.org/10.1016/j.lithos.2017.06.009.

Garzanti, E., Andò, S., 2007. Chapter 20 heavy mineral concentration in modern sands: implications for provenance interpretation. In: Developments in Sedimentology. Elsevier, pp. 517–545. https://doi.org/10.1016/S0070-4571(07)58020-9.

Götte, T., Pettke, T., Ramseyer, K., Koch-Muller, M., Mullis, J., 2011. Cathodoluminescence properties and trace element signature of hydrothermal quartz: a fingerprint of growth dynamics. Am. Mineral. 96, 802–813. https://doi.org/10.2138/am.2011.3639.

Götze, J., Plötze, M., Graupner, T., Hallbauer, D.K., Bray, C.J., 2004. Trace element incorporation into quartz: a combined study by ICP-MS, electron spin resonance, cathodoluminescence, capillary ion analysis, and gas chromatography. Geochim. Cosmochim. Acta 68 (18), 3741–3759. https://doi.org/10.1016/j.gca.2004.01.003.

Götze, J., Pan, Y., Müller, A., 2021. Mineralogy and mineral chemistry of quartz: a review. Mineral. Mag. 85, 639–664. https://doi.org/10.1180/mgm.2021.72.

Guillong, M., Meier, D., Allan, M., Heinrich, C., Yardley, B., 2008. SILLS: a MATLAB-based program for the reduction of laser ablation ICP-MS data of homogeneous materials and inclusions. In: Sylvester, P. (Ed.), Laser Ablation ICP–MS in the Earth Sciences: Current Practices and Outstanding Issues: Mineralogical Association of Canada Short Course, 40, pp. 328–333.

Günther, D., Frischknecht, R., Heinrich, C.A., Kahlert, H.-J., 1997. Capabilities of an argon fluoride 193 nm excimer laser for laser ablation inductively coupled plasma mass spectrometry microanalysis of geological materials. J. Anal. At. Spectrom. 12, 939–944. https://doi.org/10.1039/A701423F.

Handy, M.R., Zingg, A., 1991. The tectonic and rheological evolution of an attenuated cross section of the continental crust: Ivrea crustal section, southern Alps, northwestern Italy and southern Switzerland. Geol. Soc. Am. Bull. 103, 236–253. https://doi.org/10.1130/0016-7606(1991)103<0236:TTAREO>2.3.CO;2.

Haughton, P.D.W., Todd, S.P., Morton, A.C., 1991. Sedimentary provenance studies. Geol. Soc. Lond. Spec. Publ. 57, 1–11. https://doi.org/10.1144/GSL.SP.1991.057.01.01.

Hencz, M., Biró, T., Kovács, I.J., Stalder, R., Németh, K., Szakács, A., Pálos, Z., Pécskay, Z., Karátson, D., 2021. Uniform "water" content in quartz phenocrysts from silicic pyroclastic fallout deposits – implications on pre-eruptive conditions. Eur. J. Mineral. 33, 571–589. https://doi.org/10.5194/ejm-33-571-2021.

Henk, A., Franz, L., Teufel, S., Oncken, O., 1997. Magmatic underplating, extension, and crustal reequilibration: insights from a cross-section through the Ivrea zone and Strona-Ceneri zone, Northern Italy. J. Geol. 105, 367–378. https://doi.org/10.1086/515932.

Hong, J., Zhai, D., Keith, M., 2024. Quartz texture and the chemical composition fingerprint of ore-forming fluid evolution at the Bilihe porphyry Au deposit, NE China. Am. Mineral. 109, 1203–1219. https://doi.org/10.2138/am-2022-8840.

Huang, R., Audétat, A., 2012. The titanium-in-quartz (TitaniQ) thermobarometer: a critical examination and re-calibration. Geochim. Cosmochim. Acta 84, 75–89. https://doi.org/10.1016/j.gca.2012.01.009.

Huber, C., Bachmann, O., Manga, M., 2009. Homogenization processes in silicic magma chambers by stirring and mushification (latent heat buffering). Earth Planet. Sci. Lett. 283, 38–47. https://doi.org/10.1016/j.epsl.2009.03.029.

Jacamon, F., Larsen, R.B., 2009. Trace element evolution of quartz in the charnockitic Kleivan granite, SW-Norway: the Ge/Ti ratio of quartz as an index of igneous differentiation. Lithos 107, 281–291. https://doi.org/10.1016/j.lithos.2008.10.016.

Jaeger, D., Stalder, R., Masago, H., Strasser, M., 2019. OH defects in quartz as a provenance tool: application to fluvial and deep marine sediments from SW Japan. Sediment. Geol. 388, 66–80. https://doi.org/10.1016/j.sedgeo.2019.05.003.

Jafarzadeh, M., Bónová, K., Mikuš, T., Bóna, J., Rezaei-Kahkhaei, M., Taheri, A., 2021. Tourmaline and rutile geochemistry in the Early-Middle Devonian sandstones of the Padeha Formation, Alborz Range, Northern Iran. Geol. J. 56, 4645–4666. https://doi.org/10.1002/gj.4201.

Ji, G.-Y., Jiang, S.-H., Wei, H.-T., Liu, Y.-F., Yan, P.-C., 2024. Trace elements and growth patterns in quartz from the Alubaogeshan granite in the Maodeng Mo-Bi-Sn-Cu deposit, southern Great Xing'an range, NE China. Ore Geol. Rev. 165, 105864. https://doi.org/10.1016/j.oregeorev.2023.105864.

Jochum, K.P., Weis, U., Stoll, B., Kuzmin, D., Yang, Q., Raczek, I., Jacob, D.E., Stracke, A., Birbaum, K., Frick, D.A., Günther, D., Enzweiler, J., 2011. Determination of reference values for NIST SRM 610-617 glasses following ISO guidelines. Geostand. Geoanal. Res. 35, 397–429. https://doi.org/10.1111/j.1751-908X.2011.00120.x.

Jollands, M.C., Ellis, B., Tollan, P.M.E., Müntener, O., 2020a. An eruption chronometer based on experimentally determined H-Li and H-Na diffusion in quartz applied to the Bishop Tuff. Earth Planet. Sci. Lett. 551, 116560. https://doi.org/10.1016/j.epsl.2020.116560.

Jollands, M.C., Bloch, E., Müntener, O., 2020b. New Ti-in-quartz diffusivities reconcile natural Ti zoning with time scales and temperatures of upper crustal magma reservoirs. Geology 48, 654–657. https://doi.org/10.1130/G47238.1.

Jollands, M.C., Blanchard, M., Balan, E., 2020c. Structure and theoretical infrared spectra of OH defects in quartz. Eur. J. Mineral. 32, 311–323. https://doi.org/10.5194/ejm-32-311-2020.

Jollands, M.C., Tollan, P.M.E., Baumgartner, L.P., Müntener, O., 2022. Hydrogen diffusion mechanisms in quartz: insights from H–Li, ^{2}H–H and ^{2}H–H–Li exchange experiments. Mineral. Mag. 86, 112–126. https://doi.org/10.1180/mgm.2021.105.

Kamenetsky, V.S., Crawford, A.J., Meffre, S., 2001. Factors controlling chemistry of magmatic spinel: an empirical study of associated olivine, Cr-spinel and melt inclusions from primitive rocks. J. Petrol. 42, 655–671. https://doi.org/10.1093/petrology/42.4.655.

Karakas, O., Wotzlaw, J.-F., Guillong, M., Ulmer, P., Brack, P., Economos, R., Bergantz, G.W., Sinigoi, S., Bachmann, O., 2019. The pace of crustal-scale magma accretion and differentiation beneath silicic caldera volcanoes. Geology 47, 719–723. https://doi.org/10.1130/G46020.1.

Kats, A., 1962. Hydrogen in alpha quartz. Philips Res. Rep. 17, 133–279.

Keller, C.B., Schoene, B., Samperton, K.M., 2018. A stochastic sampling approach to zircon eruption age interpretation. Geochem. Perspect. Lett. 31–35. https://doi.org/10.7185/geochemlet.1826.

Keyser, W., Müller, A., Knoll, T., Menuge, J.F., Steiner, R., Berndt, J., Hart, E., Fegan, T., Harrop, J., 2023. Quartz chemistry of lithium pegmatites and its petrogenetic and economic implications: examples from Wolfsberg (Austria) and Moylisha (Ireland). Chem. Geol. 630, 121507. https://doi.org/10.1016/j.chemgeo.2023.121507.

Kronenberg, A.K., Kirby, S.H., Aines, R.D., Rossman, G.R., 1986. Solubility and diffusional uptake of hydrogen in quartz at high water pressures: implications for hydrolytic weakening. J. Geophys. Res. 91, 12723–12741. https://doi.org/10.1029/JB091iB12p12723.

Lan, Q., Lin, J., Fu, S., Luo, J., 2021. Cathodoluminescent textures and trace element signatures of hydrothermal quartz from the granite-related no. 302 uranium deposit, South China: a reconnaissance study for their genetic significances. J. Geochem. Explor. 224, 106740. https://doi.org/10.1016/j.gexplo.2021.106740.

Larsen, R.B., Henderson, I., Ihlen, P.M., Jacamon, F., 2004. Distribution and petrogenetic behaviour of trace elements in granitic pegmatite quartz from South Norway. Contrib. Mineral. Petrol. 147, 615–628. https://doi.org/10.1007/s00410-004-0580-4.

Larsen, R.B., Jacamon, F., Kronz, A., 2009. Trace element chemistry and textures of quartz during the magmatic hydrothermal transition of Oslo Rift granites. Mineral. Mag. 73, 691–707. https://doi.org/10.1180/minmag.2009.073.4.691.

Lenaz, D., Kamenetsky, V.S., Crawford, A.J., Princivalle, F., 2000. Melt inclusions in detrital spinel from the SE Alps (Italy-Slovenia): a new approach to provenance studies of sedimentary basins. Contrib. Mineral. Petrol. 139, 748–758. https://doi.org/10.1007/s004100000170.

Lenaz, D., Mazzoli, C., Velicogna, M., Princivalle, F., 2018. Trace and rare earth elements chemistry of detrital garnets in the SE Alps and Outer Dinarides flysch basins: an important tool to better define the source areas of sandstones. Mar. Pet. Geol. 98, 653–661. https://doi.org/10.1016/j.marpetgeo.2018.09.025.

Lenaz, D., Velicogna, M., Petrelli, M., Schmitz, B., 2022. The Österplana fossil meteorites and… what else? Terrestrial Cr-spinels and zircons in the Ordovician limestones of the Thorsberg Quarry (Sweden). Geosciences 12, 54. https://doi.org/10.3390/geosciences12020054.

Lenaz, D., Garlatti, G., Bernardi, F., Andò, S., 2024. Detrital tourmalines in the Cretaceous–Eocene Julian and Brkini Flysch Basins (SE Alps, Italy and Slovenia). Minerals 14, 598. https://doi.org/10.3390/min14060598.

Libowitzky, E., Rossman, G.R., 1997. An IR absorption calibration for water in minerals. Am. Mineral. 82, 1111–1115. https://doi.org/10.2138/am-1997-11-1208.

Mange, M.A., Morton, A.C., 2007. Chapter 13 geochemistry of heavy minerals. In: Developments in Sedimentology. Elsevier, pp. 345–391. https://doi.org/10.1016/S0070-4571(07)58013-1.

Monecke, T., Kempe, U., Götze, J., 2002. Genetic significance of the trace element content in metamorphic and hydrothermal quartz: a reconnaissance study. Earth Planet. Sci. Lett. 202, 709–724. https://doi.org/10.1016/S0012-821X(02)00795-1.

Müller, A., Knies, J., 2013. Trace elements and cathodoluminescence of detrital quartz in Arctic marine sediments – a new ice-rafted debris provenance proxy. Clim. Past 9, 2615–2630. https://doi.org/10.5194/cp-9-2615-2013.

Müller, A., Koch-Müller, M., 2009. Hydrogen speciation and trace element contents of igneous, hydrothermal and metamorphic quartz from Norway. Mineral. Mag. 73, 569–583. https://doi.org/10.1180/minmag.2009.073.4.569.

Müller, A., Breiter, K., Seltmann, R., Pécskay, Z., 2005. Quartz and feldspar zoning in the eastern Erzgebirge volcano-plutonic complex (Germany, Czech Republic): evidence of multiple magma mixing. Lithos 80, 201–227. https://doi.org/10.1016/j.lithos.2004.05.011.

Müller, A., Seltmann, R., Kober, B., Eklund, O., Jeffries, T., Kronz, A., 2008. Compositional zoning of Rapakivi feldspars and coexisting quartz phenocrysts. Can. Mineral. 46, 1417–1442. https://doi.org/10.3749/canmin.46.6.1417.

Müller, A., Van Den Kerkhof, A.M., Behr, H.-J., Kronz, A., Koch-Müller, M., 2009. The evolution of late-Hercynian granites and rhyolites documented by quartz – a review. Earth Environ. Sci. Trans. R. Soc. Edinb. 100, 185–204. https://doi.org/10.1017/S1755691009016144.

Müller, A., Ihlen, P.M., Snook, B., Larsen, R.B., Flem, B., Bingen, B., Williamson, B.J., 2015. The chemistry of quartz in granitic pegmatites of southern Norway: petrogenetic and economic implications. Econ. Geol. 110, 1737–1757. https://doi.org/10.2113/econgeo.110.7.1737.

Müller, A., Herklotz, G., Giegling, H., 2018. Chemistry of quartz related to the Zinnwald/Cínovec Sn-W-Li greisen-type deposit, Eastern Erzgebirge, Germany. J. Geochem. Explor. 190, 357–373. https://doi.org/10.1016/j.gexplo.2018.04.009.

Müller, A., Keyser, W., Simmons, W.B., Webber, K., Wise, M., Beurlen, H., Garate-Olave, I., Roda-Robles, E., Galliski, M.Á., 2021. Quartz chemistry of granitic pegmatites: implications for classification, genesis and exploration. Chem. Geol. 584, 120507. https://doi.org/10.1016/j.chemgeo.2021.120507.

Neukampf, J., Ellis, B.S., 2025. Lithium loss from pegmatites controlled by country rock temperature. Nat. Commun. 16, 448. https://doi.org/10.1038/s41467-024-55794-7.

Neukampf, J., Ellis, B.S., Magna, T., Laurent, O., Bachmann, O., 2019. Partitioning and isotopic fractionation of lithium in mineral phases of hot, dry rhyolites: the case of the Mesa Falls Tuff, Yellowstone. Chem. Geol. 506, 175–186. https://doi.org/10.1016/j.chemgeo.2018.12.031.

Neukampf, J., Laurent, O., Tollan, P., Bouvier, A.-S., Magna, T., Ulmer, P., France, L., Ellis, B.S., Bachmann, O., 2022. Degassing from magma reservoir to eruption in silicic systems: the Li elemental and isotopic record from rhyolitic melt inclusions and host quartz in a Yellowstone rhyolite. Geochim. Cosmochim. Acta 326, 56–76. https://doi.org/10.1016/j.gca.2022.03.037.

Niimi, N., Aikawa, N., Shinoda, K., 1999. The infrared absorption band at 3596 cm^{-1} of the recrystallized quartz from Mt. Takamiyama, Southwest Japan. Mineral. Mag. 63 (5), 693–701. https://doi.org/10.1180/002646199548853.

Pacák, K., Zachariáš, J., Strnad, L., 2019. Trace-element chemistry of barren and ore-bearing quartz of selected Au, Au-Ag and Sb-Au deposits from the Bohemian Massif. Aust. J. Geosci. 19–35. https://doi.org/10.3190/jgeosci.279.

Pereira, I., Storey, C.D., 2023. Detrital rutile: Records of the deep crust, ores and fluids. Lithos 438-439, 107010. https://doi.org/10.1016/j.lithos.2022.107010.

Peterková, T., Dolejš, D., 2019. Magmatic-hydrothermal transition of Mo-W-mineralized granite-pegmatite-greisen system recorded by trace elements in quartz: Krupka district, Eastern Krušné hory/Erzgebirge. Chem. Geol. 523, 179–202. https://doi.org/10.1016/j.chemgeo.2019.04.009.

Potrafke, A., Stalder, R., Schmidt, B.C., Ludwig, T., 2019. OH defect contents in quartz in a granitic system at 1–5 kbar. Contrib. Mineral. Petrol. 174, 98. https://doi.org/10.1007/s00410-019-1632-0.

Potrafke, A., Breiter, K., Ludwig, T., Neuser, R.D., Stalder, R., 2020. Variations of OH defects and chemical impurities in natural quartz within igneous bodies. Phys. Chem. Miner. 47, 24. https://doi.org/10.1007/s00269-020-01091-w.

Quick, J.E., Sinigoi, S., Peressini, G., Demarchi, G., Wooden, J.L., Sbisà, A., 2009. Magmatic plumbing of a large Permian caldera exposed to a depth of 25 km. Geology 37, 603–606. https://doi.org/10.1130/G30003A.1.

Rottier, B., Casanova, V., 2021. Trace element composition of quartz from porphyry systems: a tracer of the mineralizing fluid evolution. Mineral. Deposita 56, 843–862. https://doi.org/10.1007/s00126-020-01009-0.

Rottier, B., Rezeau, H., Casanova, V., Kouzmanov, K., Moritz, R., Schlöglova, K., Wälle, M., Fontboté, L., 2017. Trace element diffusion and incorporation in quartz during heating experiments. Contrib. Mineral. Petrol. 172, 23. https://doi.org/10.1007/s00410-017-1350-4.

Rottier, B., Kouzmanov, K., Casanova, V., Bouvier, A.-S., Baumgartner, L.P., Wälle, M., Fontboté, L., 2021. Tracking fluid mixing in epithermal deposits – insights from in-situ $\delta^{18}O$ and trace element composition of hydrothermal quartz from the giant Cerro de Pasco polymetallic deposit, Peru. Chem. Geol. 576, 120277. https://doi.org/10.1016/j.chemgeo.2021.120277.

Rovetta, M.R., Holloway, J.R., Blacic, J.D., 1986. Solubility of hydroxyl in natural quartz annealed in water at 900°C and 1.5 GPa. Geophys. Res. Lett. 13, 145–148. https://doi.org/10.1029/GL013i002p00145.

Rusk, B.G., Lowers, H.A., Reed, M.H., 2008. Trace elements in hydrothermal quartz: relationships to cathodoluminescent textures and insights into vein formation. Geology 36, 547. https://doi.org/10.1130/G24580A.1.

Rutter, E.H., Khazanehdari, J., Brodie, K.H., Blundell, D.J., Waltham, D.A., 1999. Synthetic seismic reflection profile through the Ivrea zone–Serie Dei Laghi continental crustal section, northwestern Italy. Geology 27, 79. https://doi.org/10.1130/0091-7613(1999)027<0079:SSRPTT>2.3.CO;2.

Saha, R., Upadhyay, D., Mishra, B., 2024. Discriminating quartz host rock based on its trace element chemistry using machine learning-a new tool for sedimentary provenance studies. Chem. Geol. 651, 122016. https://doi.org/10.1016/j.chemgeo.2024.122016.

Sbisà, A., 2009. Structure and Eruptive History of the Sesia Caldera, Northwest Italy. PhD thesis. Università degli Studi di Trieste, Italy.

Schrön, W., Schmädicke, E., Thomas, R., Schmidt, W., 1988. Geochemische Untersuchungen an Pegmatitquarzen. Z. Geol. Wiss. 16 (3), 229–244.

Shand, S.J., 1943. Eruptive Rocks: Their Genesis, Composition, Classification, and their Relation to Ore-Deposits with a Chapter on Meteorite. Wiley, New York.

Sinigoi, S., Quick, J.E., Demarchi, G., Peressini, G., 2010. The Sesia Magmatic System. J. Virtual Explor. 36. https://doi.org/10.3809/jvirtex.2010.00218.

Sinigoi, S., Quick, J.E., Demarchi, G., Klötzli, U.S., 2016. Production of hybrid granitic magma at the advancing front of basaltic underplating: inferences from the Sesia Magmatic System (South-Western Alps, Italy). Lithos 252–253, 109–122. https://doi.org/10.1016/j.lithos.2016.02.018.

Sittner, J., Götze, J., Müller, A., Renno, A.D., Ziegenrücker, R., Pan, Y., 2024. Trace element analysis and luminescence behavior of quartz in pegmatites of the Tørdal Region, Norway. Chem. Geol. 670, 122427. https://doi.org/10.1016/j.chemgeo.2024.122427.

Spencer, J.E., Doe, M.F., Domanik, K.J., 2024. Abundant 2480 Ma detrital zircons in ~1740 Ma Vishnu Schist in Northwestern Arizona: derivation from the Matachewan Large Igneous Province? Am. J. Sci. 324. https://doi.org/10.2475/001c.115633.

Stalder, R., 2014. OH-defect content in detrital quartz grains as an archive for crystallisation conditions. Sediment. Geol. 307, 1–6. https://doi.org/10.1016/j.sedgeo.2014.04.002.

Stalder, R., 2021. OH point defects in quartz – a review. Eur. J. Mineral. 33, 145–163. https://doi.org/10.5194/ejm-33-145-2021.

Stalder, R., Konzett, J., 2012. OH defects in quartz in the system quartz–albite–water and granite–water between 5 and 25 kbar. Phys. Chem. Miner. 39, 817–827. https://doi.org/10.1007/s00269-012-0537-5.

Stalder, R., Neuser, R.D., 2013. OH-defects in detrital quartz grains: potential for application as tool for provenance analysis and overview over crustal average. Sediment. Geol. 294, 118–126. https://doi.org/10.1016/j.sedgeo.2013.05.013.

Stalder, R., Potrafke, A., Billström, K., Skogby, H., Meinhold, G., Gögele, C., Berberich, T., 2017. OH defects in quartz as monitor for igneous, metamorphic, and sedimentary processes. Am. Mineral. 102, 1832–1842. https://doi.org/10.2138/am-2017-6107.

Stalder, R., Von Eynatten, H., Costamoling, J., Potrafke, A., Dunkl, I., Meinhold, G., 2019. OH in detrital quartz grains as tool for provenance analysis: Case studies on various settings from Cambrian to recent. Sediment. Geol. 389, 121–126. https://doi.org/10.1016/j.sedgeo.2019.06.001.

Suttner, L.J., Leininger, R.K., 1972. Comparison of the trace element content of plutonic, volcanic, and metamorphic quartz from Southwestern Montana. Geol. Soc. Am. Bull. 83, 1855–1862. https://doi.org/10.1130/0016-7606(1972)83[1855:COTTEC]2.0.CO;2.

Suzuki, S., Nakashima, S., 1999. In-situ IR measurements of OH species in quartz at high temperatures. Phys. Chem. Miner. 26, 217–225. https://doi.org/10.1007/s002690050180.

Szymanowski, D., Wotzlaw, J.-F., Ellis, B.S., Bachmann, O., Guillong, M., von Quadt, A., 2017. Protracted near-solidus storage and pre-eruptive rejuvenation of large magma reservoirs. Nat. Geosci. 10, 777–782. https://doi.org/10.1038/ngeo3020.

Szymanowski, D., Ellis, B.S., Wotzlaw, J.-F., Bachmann, O., 2019. Maturation and rejuvenation of a silicic magma reservoir: high-resolution chronology of the Kneeling Nun Tuff. Earth Planet. Sci. Lett. 510, 103–115. https://doi.org/10.1016/j.epsl.2019.01.007.

Tailby, N.D., Cherniak, D.J., Watson, E.B., 2018. Al diffusion in quartz. Am. Mineral. 103, 839–847. https://doi.org/10.2138/am-2018-5613.

Takahashi, R., Matsueda, H., Okrugin, V.M., Ono, S., 2007. Epithermal gold-silver mineralization of the Asachinskoe deposit in South Kamchatka, Russia. Resour. Geol. 57, 354–373. https://doi.org/10.1111/j.1751-3928.2007.00034.x.

Tavazzani, L., Peres, S., Sinigoi, S., Demarchi, G., Musumeci, G., 2017. Structure and petrography of the Valle Mosso pluton, Sesia Magmatic System, Southern Alps. J. Maps 13, 684–697. https://doi.org/10.1080/17445647.2017.1354787.

Tavazzani, L., Peres, S., Sinigoi, S., Demarchi, G., Economos, R.C., Quick, J.E., 2020. Timescales and mechanisms of crystal-mush rejuvenation and melt extraction recorded in Permian plutonic and volcanic rocks of the Sesia Magmatic System (Southern Alps, Italy). J. Petrol. 61, egaa049. https://doi.org/10.1093/petrology/egaa049.

Tavazzani, L., Wotzlaw, J.-F., Economos, R., Sinigoi, S., Demarchi, G., Szymanowski, D., Laurent, O., Bachmann, O., Chelle-Michou, C., 2023. High-precision zircon age spectra record the dynamics and evolution of large open-system silicic magma reservoirs. Earth Planet. Sci. Lett. 623, 118432. https://doi.org/10.1016/j.epsl.2023.118432.

Tavazzani, L., Economos, R.C., Peres, S., Demarchi, G., Sinigoi, S., Bachmann, O., 2024. The role of latent heat buffering in the generation of high-silica rhyolites. J. Petrol. 65, egae072. https://doi.org/10.1093/petrology/egae072.

Thomas, S.M., Koch-Müller, M., Reichart, P., Rhede, D., Thomas, R., Wirth, R., Matsyuk, S., 2009. IR calibrations for water determination in olivine, r-GeO2, and SiO2 polymorphs. Phys. Chem. Miner. 36, 489–509. https://doi.org/10.1007/s00269-009-0295-1.

Thomas, J.B., Bruce Watson, E., Spear, F.S., Shemella, P.T., Nayak, S.K., Lanzirotti, A., 2010. TitaniQ under pressure: the effect of pressure and temperature on the solubility of Ti in quartz. Contrib. Mineral. Petrol. 160, 743–759. https://doi.org/10.1007/s00410-010-0505-3.

Tollan, P., Ellis, B., Troch, J., Neukampf, J., 2019. Assessing magmatic volatile equilibria through FTIR spectroscopy of unexposed melt inclusions and their host quartz: a new technique and application to the Mesa Falls Tuff, Yellowstone. Contrib. Mineral. Petrol. 174, 24. https://doi.org/10.1007/s00410-019-1561-y.

Triebold, S., von Eynatten, H., Zack, T., 2012. A recipe for the use of rutile in sedimentary provenance analysis. Sediment. Geol. 282, 268–275. https://doi.org/10.1016/j.sedgeo.2012.09.008.

Troch, J., Huber, C., Bachmann, O., 2022. The physical and chemical evolution of magmatic fluids in near-solidus silicic magma reservoirs: implications for the formation of pegmatites. Am. Mineral. 107, 190–205. https://doi.org/10.2138/am-2021-7915.

Wang, Y., Qiu, K., Müller, A., Hou, Z., Zhu, Z., Yu, H., 2021. Machine learning prediction of quartz forming-environments. J. Geophys. Res. Solid Earth 126, e2021JB021925. https://doi.org/10.1029/2021JB021925.

Wark, D.A., Watson, E.B., 2006. TitaniQ: a titanium-in-quartz geothermometer. Contrib. Mineral. Petrol. 152, 743–754. https://doi.org/10.1007/s00410-006-0132-1.

Weltje, G.J., Von Eynatten, H., 2004. Quantitative provenance analysis of sediments: review and outlook. Sediment. Geol. 171, 1–11. https://doi.org/10.1016/j.sedgeo.2004.05.007.

Wotzlaw, J.-F., Schaltegger, U., Frick, D.A., Dungan, M.A., Gerdes, A., Günther, D., 2013. Tracking the evolution of large-volume silicic magma reservoirs from assembly to supereruption. Geology 41, 867–870. https://doi.org/10.1130/G34366.1.

Zezza, U., 1977. Studio petrografico del massiccio granitico del Biellese. In: Atti Società Italiana Scienze Naturali, Museo Civico Storia Naturale Milano, 118, pp. 65–102.

Zhang, W., Terry Chen, W., Zhang, X.-C., Tang, Y.-W., 2022. The trace element chemistry of quartz in carbonatite-related REE deposits: implication for REE exploration. Ore Geol. Rev. 149, 105068. https://doi.org/10.1016/j.oregeorev.2022.105068.

Zhou, H., Müller, A., Berndt, J., 2023. Quartz chemistry fingerprints melt evolution and metamorphic modifications in high-purity quartz deposits. Geochim. Cosmochim. Acta 356, 179–195. https://doi.org/10.1016/j.gca.2023.07.015.

Zhou, J., Wang, Q., Wang, H., Ma, J., Zhu, G., Zhang, L., 2025. Pegmatite lithium deposits formed within low-temperature country rocks. Nat. Commun. 16, 447. https://doi.org/10.1038/s41467-024-55793-8.